Cell Reports

Article

Fear memory-associated synaptic and mitochondrial changes revealed by deep learning-based processing of electron microscopy data

Graphical abstract

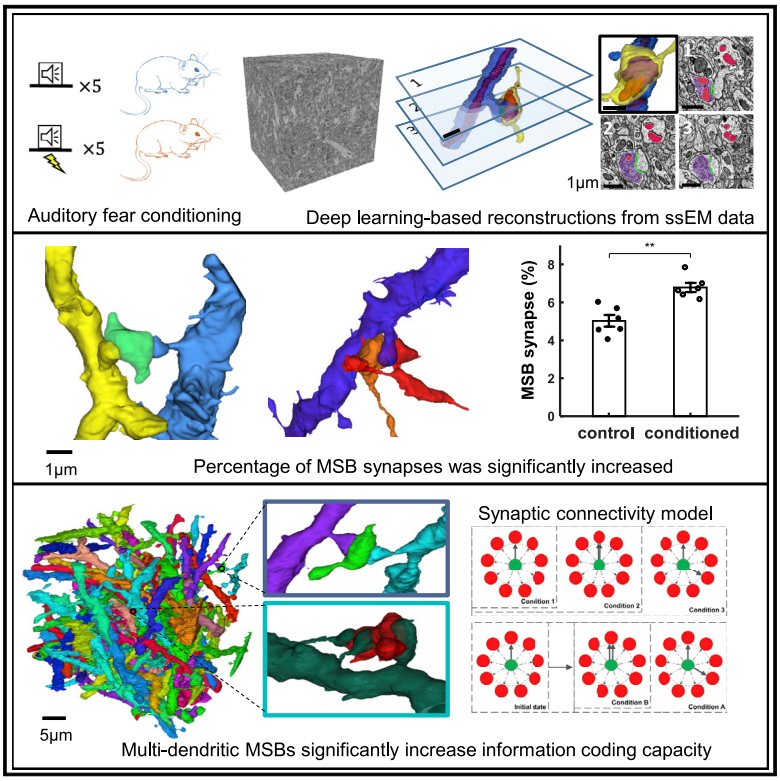

Highlights

- A deep learning pipeline for identifying cellular compartments from EM images
- Auditory fear learning increases the number and decreases the size of mitochondria
- Auditory fear learning promotes multi-synaptic bouton formation in auditory cortex
- Multi-dendritic connections increase information storage capacity by over 50%

Authors

Jing Liu, Junqian Qi, Xi Chen, ..., Qiwei Xie, Hua Han, Yang Yang

Correspondence

qiwei.xie@bjut.edu.cn (Q.X.),
hua.han@ia.ac.cn (H.H.),
yangyang2@shanghaitech.edu.cn (Y.Y.)

In brief

Liu et al. developed a deep learning method to automatically identify and reconstruct synapses and mitochondria from EM images of the mouse auditory cortex, revealing fear learning-associated subcellular modifications. Mathematical modeling suggests that the synaptic reconfiguration can increase information storage capacity.

Liu et al., 2022, Cell Reports *40*, 111151
August 2, 2022
https://doi.org/10.1016/j.celrep.2022.111151

CellPress

Cell Reports

CellPress
OPEN ACCESS

Article

Fear memory-associated synaptic and mitochondrial changes revealed by deep learning-based processing of electron microscopy data

Jing Liu,[1,2,7] Junqian Qi,[3,4,5,7] Xi Chen,[1,7] Zhenchen Li,[1,2,7] Bei Hong,[1,2] Hongtu Ma,[1] Guoqing Li,[1] Lijun Shen,[1] Danqian Liu,[4] Yu Kong,[4] Hao Zhai,[1,2] Qiwei Xie,[6,*] Hua Han,[1,2,4,*] and Yang Yang[3,8,*]

[1]National Laboratory of Pattern Recognition, Research Center for Brain-inspired Intelligence, Institute of Automation, Chinese Academy of Sciences, Beijing 100190, China
[2]School of Artificial Intelligence, School of Future Technology, University of the Chinese Academy of Sciences, Beijing 101408, China
[3]School of Life Science and Technology, ShanghaiTech University, Shanghai, China
[4]Institute of Neuroscience, State Key Laboratory of Neuroscience, Key Laboratory of Primate Neurobiology, Center for Excellence in Brain Science and Intelligence Technology, Chinese Academy of Sciences, Shanghai 200031, China
[5]University of the Chinese Academy of Sciences, Beijing 100049, China
[6]Research Base of Beijing Modern Manufacturing Development, Beijing University of Technology, Beijing 100124, China
[7]These authors contributed equally
[8]Lead contact
*Correspondence: qiwei.xie@bjut.edu.cn (Q.X.), hua.han@ia.ac.cn (H.H.), yangyang2@shanghaitech.edu.cn (Y.Y.)
https://doi.org/10.1016/j.celrep.2022.111151

SUMMARY

Serial section electron microscopy (ssEM) can provide comprehensive 3D ultrastructural information of the brain with exceptional computational cost. Targeted reconstruction of subcellular structures from ssEM datasets is less computationally demanding but still highly informative. We thus developed a region-CNN-based deep learning method to identify, segment, and reconstruct synapses and mitochondria to explore the structural plasticity of synapses and mitochondria in the auditory cortex of mice subjected to fear conditioning. Upon reconstructing over 135,000 mitochondria and 160,000 synapses, we find that fear conditioning significantly increases the number of mitochondria but decreases their size and promotes formation of multi-contact synapses, comprising a single axonal bouton and multiple postsynaptic sites from different dendrites. Modeling indicates that such multi-contact configuration increases the information storage capacity of new synapses by over 50%. With high accuracy and speed in reconstruction, our method yields structural and functional insight into cellular plasticity associated with fear learning.

INTRODUCTION

The mammalian brain consists of a vast and complex network of neurons interconnected by specialized sites called synapses (Gray, 1959, 1969; Holtmaat and Svoboda, 2009; Yuste, 2015). In this network, a neuron may receive input from, and send output to, thousands of other neurons. The concerted activities of neurons, which encode, process, and store information, fundamentally depend on the connectivity patterns of synapses (Spruston, 2008; Stepanyants et al., 2002). Thus, it is critical to elucidate the organization of synaptic circuits to understand brain functions. Light microscopy has been used to examine populations of synapses *in vitro* and *in vivo*. Previous work has shown that learning effectively modifies synaptic structures of the mammalian cerebral cortex (Frank et al., 2018; Hayashi-Takagi et al., 2015; Holtmaat and Svoboda, 2009; Moczulska et al., 2013; Xu et al., 2009; Yang et al., 2009, 2016). Auditory fear conditioning (AFC), a common paradigm of associative learning, increases formation of presynaptic boutons and postsynaptic spines in the auditory cortex (primary auditory cortex [A1]) (Moczulska et al., 2013; Yang et al., 2016). However, although boutons and spines can be visualized using light microscopy, the width of the synaptic cleft is below the diffraction limit, and synapses are difficult to discern using light microscopy images (Schoonover et al., 2014). The serial section electron microscopy (ssEM) technique (Hayworth et al., 2014) overcomes the resolution problem and enables large-scale 3D reconstruction of brain tissue with nanometer-scale resolution, which is sufficient to resolve the ultrastructural features of synapses, such as presynaptic vesicles, the synaptic cleft, and the postsynaptic density (PSD) (Kim et al., 2018; Rollenhagen et al., 2007, 2015; Satzler et al., 2002; Schmuhl-Giesen et al., 2022; Xu-Friedman and Regehr, 2003; Yakoubi et al., 2019a, 2019b). However, manual identification and segmentation of a large number of synapses from massive ssEM datasets is extremely time consuming. Thus, automated analysis pipelines are much desired (Jagadeesh et al., 2014; Kreshuk et al., 2011; Rodriguez-Moreno et al., 2018; Shapson-Coe et al., 2021).

To date, a variety of machine learning-based approaches for synapse detection have been proposed. Some methods require

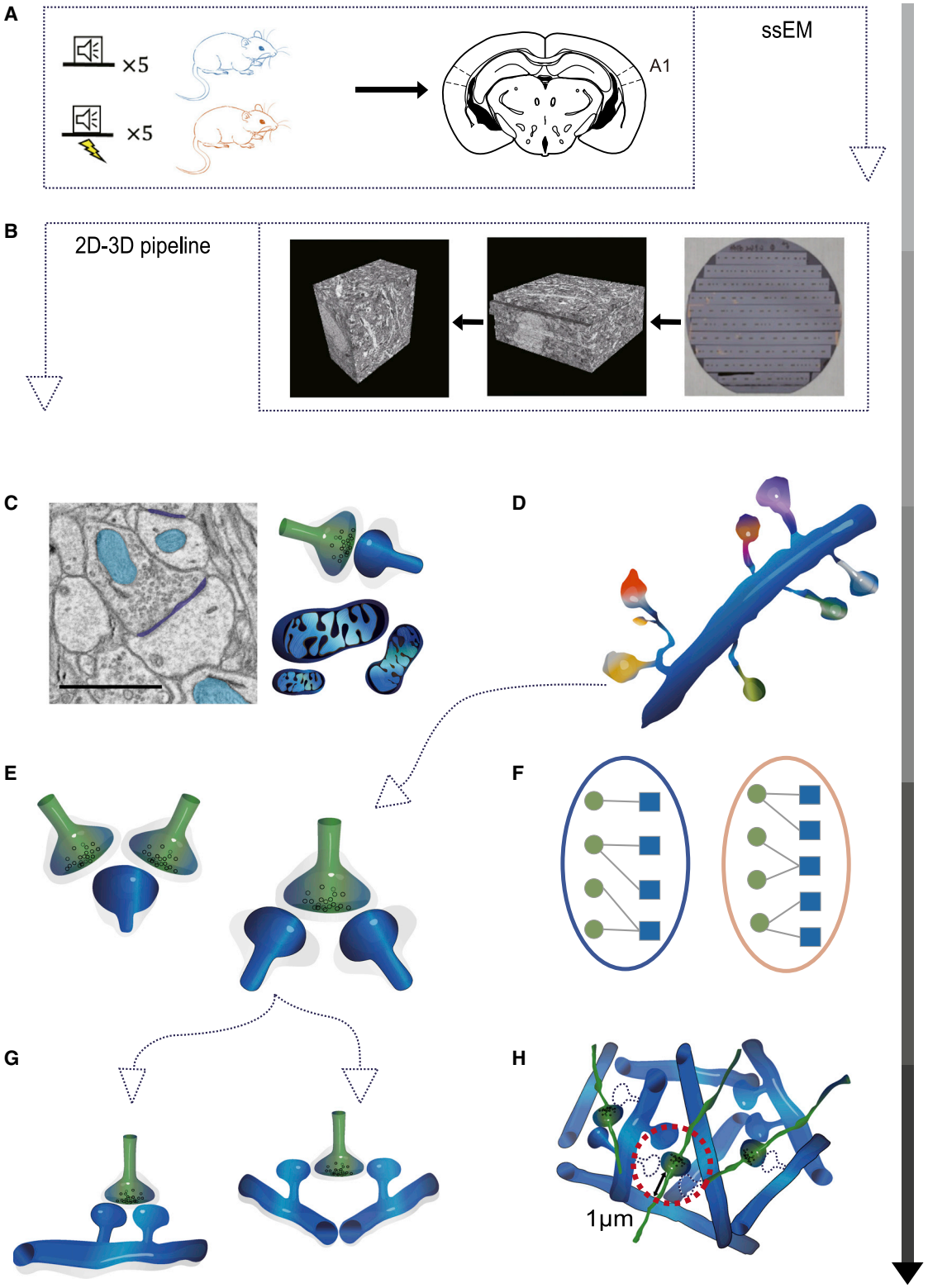

Figure 1. Schematic of the experimental procedure

(A) AFC and sample preparation. Control mice are subjected to 5 repeats of tone pips; fear-conditioned mice are subjected to 5 repeats of paired tone pips and foot shocks. 4 days after conditioning, auditory cortex (A1) tissue blocks are harvested from these mice and prepared for serial section electron microscopy (ssEM).

(legend continued on next page)

saturated reconstruction or segmentation of neuronal structures prior to synapse detection (Mishchenko et al., 2010; Staffler et al., 2017), which is daunting for large datasets. Some methods do not make full use of the contextual information or structural properties of synapses (Jagadeesh et al., 2014; Kreshuk et al., 2011), making them more prone to errors. Some other methods require nearly isotropic imaging data (Dorkenwald et al., 2017), a requirement incompatible with standard ssEM, in which the axial resolution (section thickness) is typically much worse than the lateral resolution. Most recently, an indirect method detected synapses by identifying the synaptic connectivity (pre- and postsynaptic component of each synapse) (Shapson-Coe et al., 2021).

Mitochondria play essential roles in cellular functions, such as producing adenosine triphosphate (ATP) and participating in calcium homeostasis (Friedman and Nunnari, 2014; Ly and Verstreken, 2006; Mironov, 2007; Mironov et al., 2005). Synaptic mitochondria are linked to the process of neurotransmitter release and organization of synaptic vesicles (Mironov and Symonchuk, 2006; Verstreken et al., 2005; Vos et al., 2010). In the past decade, ssEM has been increasingly used to investigate mitochondrial structures. Along with this, a variety of automated methods have been developed to detect mitochondria from ssEM images. One method was based on handcrafted features and traditional classifiers (Lucchi et al., 2011, 2014; Narasimha et al., 2009) and the other on powerful 2D or 3D convolutional neural networks (CNNs) (Dorkenwald et al., 2017; Oztel et al., 2017).

In this study, we used region-CNN (R-CNN)-based deep learning algorithms to identify, segment, and reconstruct synapses and mitochondria from ssEM images of the mouse auditory cortex. Our pipeline achieved state-of-the-art accuracy with a speed almost three orders of magnitude faster than human experts, enabling us to sample more than 100,000 synapses and mitochondria. Using this method, we studied how a classic learning model, AFC, affects the synaptic and mitochondrial organization in the A1 (Figures 1 and S1A). Using automated synapse reconstruction and mathematical modeling, we found that AFC increases multi-synaptic boutons connecting one axonal bouton to multiple different dendrites in the A1 and that these 1-to-N connections dramatically increased the information coding capacity, possibly representing a synaptic memory engram.

RESULTS

AFC as a model for learning and memory

To investigate changes in cellular structures induced by learning and memory in the adult brain, we used a simple and robust behavioral model for associative learning: AFC. Specifically, conditioned mice received 5 sessions of paired tone pips (14 kHz, 10 s, conditioned stimulus [CS]) and foot shocks (0.6 mA, 2 s, unconditioned stimulus [US]), whereas control mice received 5 sessions of just tone pips (Figure 1A; see STAR Methods for details). Mice were tested with the CS 24 h after conditioning. All conditioned mice (n = 3) exhibited high freezing responses, whereas all control mice (n = 3) exhibited low freezing responses (Figure S1B). 4 days after conditioning, we harvested auditory cortex (A1) tissue blocks from these mice and prepared them for ssEM (Figure 1B). We sectioned a total of 2.8×10^5 μm^3 A1 tissue at 50-nm section thickness and imaged at 2- to 4-nm lateral resolution (Video S1).

Deep learning-based reconstruction of synapses in the A1

We first explored the synaptic changes associated with AFC by extracting structural information of synapses from ssEM data. Synapses have distinct ultrastructural properties: the pre- and postsynaptic apposition zone contains a presynaptic element composed of a pool of synaptic vesicles (Imbrosci et al., 2022), a synaptic cleft of variable width, and a PSD on the postsynaptic element. These special features enabled us to design a 2D-3D pipeline to detect and reconstruct synapses at the 2D and 3D levels. Because of the high anisotropy of voxels (x-y resolution, 2–4 nm; z, 50 nm) and intrinsic local misalignments in most ssEM data, using a 3D CNN increases the computational complexity without offering any improvement in performance. Therefore, we used the Mask R-CNN (He et al., 2017) model at the 2D level to detect and segment synapses in each 2D image (Figure 2A). The Mask R-CNN is a deep neural network for the instance segmentation task that can separate distinct objects in an image. As illustrated in Figure 2B, Mask R-CNN is composed of three primary parts: the backbone network, region proposal network (RPN), and R-CNN. The backbone network provides shared feature maps for the other two parts. The backbone used for synapse detection is a Feature Pyramid Network (FPN; Figure 2B; STAR Methods; Lin et al., 2017), which we

(B) The ssEM image acquisition and alignment procedure. Serial sections are automatically sectioned using an automated tape-collecting ultramicrotome (ATUM); these are collected onto 4-in silicon wafers. The wafers are then imaged using scanning EM. Raw images are aligned using a scale invariant feature transform (SIFT) flow-based, non-linear registration algorithm.
(C) Identification of synapses and mitochondria in the A1. Synapses and mitochondria are automatically identified using our 2D-3D pipeline based on the region-convolutional neural network (R-CNN). Scale bar, 1 μm.
(D) Reconstructed dendrites from the saturated reconstruction by applying the Multicut pipeline (Beier et al., 2017). The spine fragments are manually traced to the original dendrite.
(E) Multiple-contact synapse (MCS) localization and classification. MCSs are manually verified and classified into multi-synaptic boutons (MSBs; consisting of a single bouton contacting multiple PSDs) and multi-synaptic spines (MSSs; consisting of a single spine contacting multiple boutons) by incorporating the vesicle cloud features.
(F) A combinatorial mathematical model is built to simulate the synaptic turnover associated with the fear-conditioning process.
(G) MSB subtypes. MSBs are classified into single- or multi-dendritic MSBs by incorporating saturated reconstructions to identify the origination dendrites of multiple postsynaptic spines.
(H) A synaptic network is built based on ssEM data using the number of dendrites within a 1-μm radius around a bouton.
See also Figure S1 and Table S1.

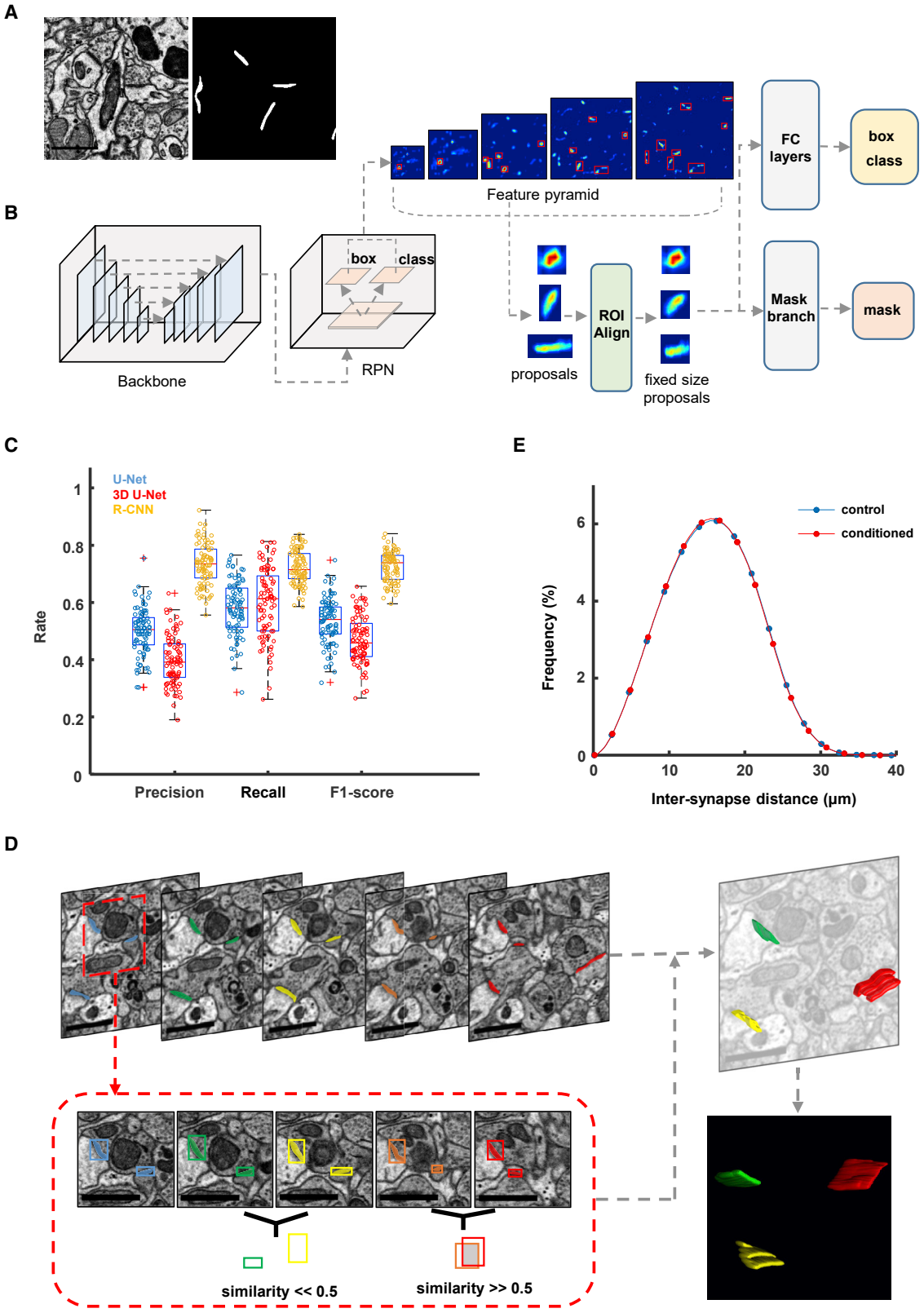

(legend on next page)

modified from the ResNet50 model (He et al., 2016). As a typical two-stage detector, it first generates enough region proposals to guarantee the pre-specified recall rate with an RPN. Subsequently, the feature maps of the proposals are extracted as regions of interest (ROIs). R-CNN then makes further classification (predicting the scores being synapses or not) and regression (predicting the coordinates of synapses' bounding boxes) and predicts a pixel-level mask for the ROIs identified in the first stage. The classification branch that predicted each ROI as a synaptic or non-synaptic object explored the features of the synaptic vesicles and the PSD. This second stage guarantees the precision rate. After obtaining the final positions, the mask branch predicted the segmentation masks of the detected PSDs.

To train the network, a total of 600 ssEM images from the aforementioned mouse A1 dataset were annotated by two expert annotators with cross-validation (two volumes of 2,048 × 2,048 × 300 voxels for the control and conditioned groups, respectively), which was split into training (60%), validation (20%), or test (20%) sets. Evaluation against the test set showed that our pipeline achieved a 0.90 precision rate and a 0.83 recall rate for synapse detection (Figures S2A and S2B). Experiments run on different sizes of labeled data demonstrated the effectiveness and robustness of the model (Figure S2C).

To quantitatively evaluate the performance (efficiency and accuracy) of the Mask R-CNN, we compared it with other state-of-the-art CNNs (Figures S2D–S2F) using a previously reported public ssEM dataset (Xiao et al., 2018) comprising 178 slices sized 8,576 × 7,616 pixels. The dataset is divided into two equal parts: one for training and one for testing. The baseline network U-Net (Ronneberger et al., 2015) and the 3D U-Net (Çiçek et al., 2016) are commonly used for biomedical image segmentation tasks. To comprehensively evaluate the performance of the three networks, we plotted precision-recall (PR) curves across different detection and segmentation thresholds (Figures S2G and S2H). For detection, Mask R-CNN is far superior to U-Net and 3D U-Net in terms of F1 score (the harmonic mean of precision and recall), precision rate, and recall rate (Figure 2C). For segmentation, Mask R-CNN shows performance comparable with U-Net and 3D U-Net at threshold of less than 0.6 (Figure S2H). We also compared the model complexity by computing floating point operations (FLOPs) and number of trainable parameters (Figure S2I).

At the 3D level, we used a 3D connection algorithm (Figure 2D) to find the instance-level connected components and reconstruct synapses. Based on the continuity of the aligned ssEM volume and the spatial structure of the synapses, we constructed similarity matrices (STAR Methods) between adjacent layers with synapse detection boxes. When the similarity of the two bounding boxes was greater than a certain threshold (T_s; default set at 0.5), we considered the corresponding synapse to be the same one at the 3D level. When a synapse appeared in T_k (default set as 3; Figure S3A) continuous layers or more, it was retained and given a unique label; otherwise, it was discarded as a false positive. This connection algorithm was also used as a post-processing method to remove false positives and refine the segmentation and detection results. After connected component labeling, we could obtain the synaptic instance segmentation results, where each label indicated a unique synapse in 3D.

Using our 2D-3D pipeline, we automatically identified, segmented, and reconstructed over 160,000 synapses from 14 A1 tissue blocks of 6 mice (Figures S3B and S3C; Video S1; Table S1). We computed the Euclidean distances between any two synapses and found that synapses were uniformly distributed in control and conditioned animals (Figure 2E).

Deep learning-based reconstruction of mitochondria in the A1

We designed our 2D-3D pipeline so that it is capable of identifying any cellular compartment or organelle with borders and distinct structural properties. To demonstrate its versatility, we used this pipeline to identify mitochondria, the major energy source for cellular functions and neuronal activities, from the same ssEM dataset. Mask R-CNN first predicted a binary mitochondrial mask (Figure 3A) for each input image, after which the 3D connection algorithm produced the reconstructed mitochondria (Figure 3B). To build a ground truth mitochondrion dataset, mitochondria from 20 images (7,492 × 7,492 pixels) were labeled by experienced annotators. The train-validation-test split ratio used here was the same as for synapses. To correct for discrepancies in imaging conditions, we preprocessed the images using histogram matching. The images were cropped into smaller patches (1,024 × 1,024 pixels) for training the R-CNN. The proposed algorithm achieved a 0.93 precision rate and a 0.91 recall rate for mitochondrion detection on the test set (Figure S3D). To comprehensively evaluate model performance, we also plotted PR curves across different detection and segmentation thresholds (Figures S3E and S3F).

After validation against the ground truth dataset, we applied the 2D-3D pipeline to examine mitochondrial changes after AFC. We identified, segmented, and reconstructed over 135,000 mitochondria from 14 A1 tissue blocks of 6 mice (Figure 3C; Video S1). Previous work has established that, in neurons, mitochondria could be found in presynaptic boutons and

Figure 2. Automated identification and reconstruction of synapses

(A) Examples of an EM image and a binary synaptic mask predicted by Mask R-CNN. Scale bar, 1 μm.

(B) Network architecture of Mask R-CNN, which takes a 1,024 × 1,024 image patch as input and puts out the bounding boxes and binary masks of all synapses in the input image.

(C) Comparison with other state-of-the-art methods in terms of precision, recall, and F1 score metrics on a public ssEM dataset. Each circle indicates an image from the test sets (half of this public ssEM dataset). n = 89 images.

(D) Sketch of the similarity-index-based 3D connection algorithm used for reconstructing synapses. The similarity of two synapses from adjacent layers depends on the intersection over union of the bounding boxes. Scale bar, 1 μm.

(E) Normalized histograms of Euclidean distances between any two synapses in control (blue) and conditioned mice (red); these accord with a normal distribution (control: p = 0.1149, two-sided Kolmogorov-Smirnov test; conditioned: p = 0.4801, two-sided Kolmogorov-Smirnov test).

See also Figures S2, S3 and Video S1.

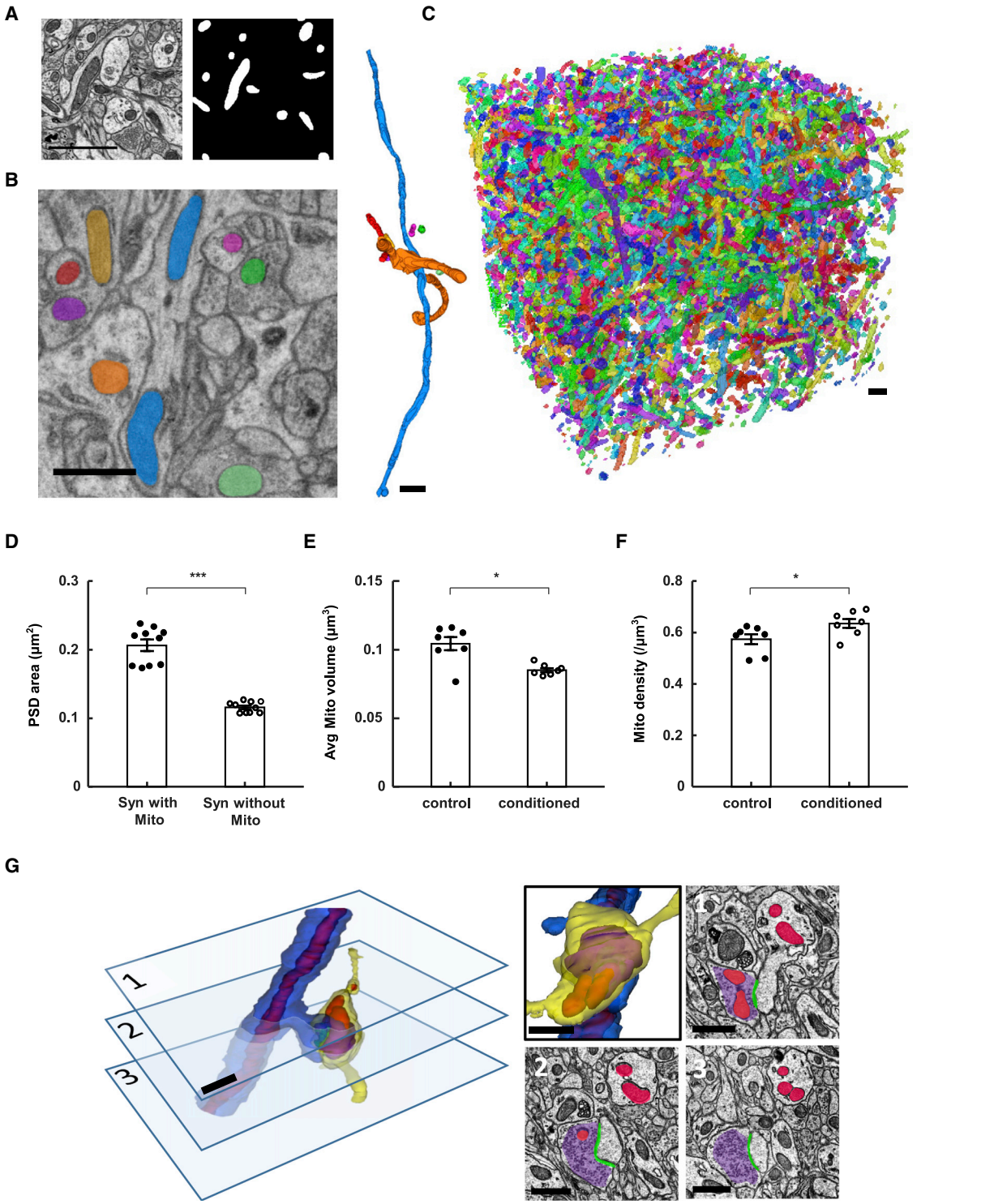

Figure 3. Automated identification of mitochondria and vesicle clouds

(A) Examples of an EM image and a binary mitochondrial mask predicted by Mask R-CNN. Scale bar, 1 μm.

(B) EM image and 3D visualization of 8 mitochondria located in dendrites or axons. Scale bar, 1 μm.

(C) 3D visualization of all mitochondria from one 22 × 24 × 25-μm image stack. Scale bar, 1 μm.

(D) The postsynaptic density (PSD) area (0.21 ± 0.008 μm^2) of synapses containing mitochondria in the presynaptic boutons is larger than the PSD area (0.12 ± 0.002 μm^2) of synapses without mitochondria in the presynaptic boutons. n = 10 blocks, Mann-Whitney U test, $p < 0.001$.

(legend continued on next page)

dendritic shafts but not postsynaptic spines (Kasthuri et al., 2015). By combining the synapse dataset and mitochondrion dataset, we found that synapses with presynaptic mitochondria had larger PSDs than those without (PSD size with presynaptic mitochondria, 0.21 ± 0.008 μm^2; PSD size without, 0.12 ± 0.002 μm^2; Mann-Whitney U test, p = 0.0002; Figure 3D). AFC significantly decreased mitochondrial volumes (control, 0.10 ± 0.005 μm^3; conditioned, 0.09 ± 0.001 μm^3; Mann-Whitney U test, p = 0.0262; Figure 3E) but increased mitochondrial density (control, 0.57 ± 0. 019 per μm^3; conditioned, 0.64 ± 0. 017 per μm^3; Mann-Whitney U test, p = 0.0379; Figure 3F). Thus, although AFC does not alter the spatial distribution of synapses, it increases the number and decreases the size of mitochondria, suggesting that mitochondrial fission may accompany AFC.

A synapse dataset combined with mitochondria and synaptic vesicles

We successfully identified and reconstructed the PSDs of synapses from ssEM images with our 2D-3D pipeline, but the direction of the synaptic connectivity is still unclear. Vesicle clouds in the presynaptic terminals provide essential information for distinguishing axons from dendrites in ssEM images. Thus, we applied FusionNet (Quan et al., 2021), a variant of U-Net, to detect synaptic vesicle clouds (Figure S3G). FusionNet used residual blocks and summation-based skip connections (Figure S3H), which could achieve state-of-the-art performance in segmenting the ssEM data. The network predicted probability maps, with each element indicating the probability of belonging to the foreground. Synaptic vesicles were about 35–40 nm in diameter and concentrated in the presynaptic terminal. Because labeling each synaptic vesicle is extremely time consuming, we annotated vesicle clouds to reduce the annotation workload. We extracted two volumes (2,048 × 2,048 × 50 voxels) for synaptic vesicle annotation and divided them into training, validation, and test sets using the same split ratio as for synapses and mitochondria. To evaluate performance on the test set, a thresholding operation was conducted, and FusionNet yielded a precision rate of 0.83 and a recall rate of 0.80 (Figure S3I).

After applying the trained version of FusionNet to identify vesicle clouds in the A1 (Figure S3J), we constructed a large-scale dataset containing synapses, mitochondria, and vesicle clouds from control and conditioned mice, which can be used for studying the cellular ultrastructural changes associated with AFC (Video S1). An example showing the synaptic ultrastructure, including the synaptic cleft, mitochondria, and vesicle cloud, is presented in Figure 3G.

Fear conditioning increased a specific type of multi-contact synapses

Synapses that form 1-to-N or N-to-1 connections, termed multiple-contact synapses (MCSs), have been observed in the brains of mice, rabbits and monkeys (Jones et al., 1997; Sorra and Harris, 1993; Woolley et al., 1996) and are implicated in functions such as eye-blink conditioning (Geinisman et al., 2001). Statistical and structural analyses are limited because of the small sample size obtained by manual notation of EM data in previous studies. In our previous work, we found that, in the adult mouse A1, synaptogenesis rarely occurs *de novo* but, rather, by addition of new boutons or spines to existing synapses, termed the "partial addition rule" (Yang et al., 2016). The finding that AFC leads to an increase in spine and bouton formation together with this rule may lead to an increase in MCSs if the additions are not accompanied by elimination of existing synapses via synaptic replacement.

To find out whether MCSs serve as a synaptic memory engram for AFC, we designed a semi-automated method to localize all MCSs in the tissue blocks to examine MCSs at a large scale (Figures 4A and S4A–S4C). To identify MCSs from annotated synapses, we took advantage of the fact that MCSs share a bouton or a PSD, so the distances of PSDs or boutons of one MCS are restricted to the size of a synapse (~1 μm). Based on this information, the candidate MCSs were detected by restricting the distances between identified synapses. Then expert annotators proofread to exclude false positives (Figure 4B), which were not easily distinguished in 2D images. By combining the segmentation results of synapses and vesicle clouds to estimate the number of boutons in one MCS, we then classified all the identified MCSs into two types: those consisting of a single bouton contacting multiple PSDs (multi-synaptic bouton [MSB]; Figures 4C and 4D; Video S2) or those consisting of a single spine contacting multiple boutons (multi-synaptic spine [MSS]; Figure 4E; Video S2).

We found that the percentage of MSB synapses was significantly increased after AFC (control, 5.0% ± 0.3%; conditioned, 6.8% ± 0.2%; Mann-Whitney U test, p = 0.0022; Figure 4F), whereas that of MSS synapses did not change (control, 1.8% ± 0.4%; conditioned, 1.4% ± 0.3%; Mann-Whitney U test, p = 0.5887; Figure 4G). We also noted that the majority (~98.58% ± 0.4%) of MSBs had 2 postsynaptic targets, but a few had 3 or more (Figure 4D), and the percentage of MSBs forming more than 2 synapses was significantly elevated in the conditioned animals (control, 1.07% ± 0.3%; conditioned, 2.26% ± 0.2%; Mann-Whitney U test, p = 0.0087; Figure S4D). These results showed that AFC affected MCSs specifically by promoting formation of MSBs. We also found that the percentage of MSB synapses with presynaptic mitochondria is significantly higher than that of single-synaptic-bouton (SSB) synapses with presynaptic mitochondria (MSB, 59.41% ± 1.3%; SSB, 34.12% ± 0.6%; Mann-Whitney U test, p = 0.0002; Figure 4H), suggesting that MSBs are more energy demanding.

(E) The average mitochondrial volume is smaller in conditioned mice (0.09 ± 0.001 μm^3) than in controls (0.10 ± 0.005 μm^3). n = 7 blocks, Mann-Whitney U test, $p < 0.05$.
(F) The mitochondrial density is higher in conditioned mice (0.64 ± 0.017/μm^3) than in controls (0.57 ± 0.019/μm^3). n = 7 blocks, Mann-Whitney U test, $p < 0.05$.
(G) A typical example of a spine synapse with the identified PSD (green), mitochondria (red), and vesicle cloud (purple). Another view and the corresponding EM images are displayed on the right. Scale bar, 1 μm.
See also Figure S3, Table S1, and Video S1.

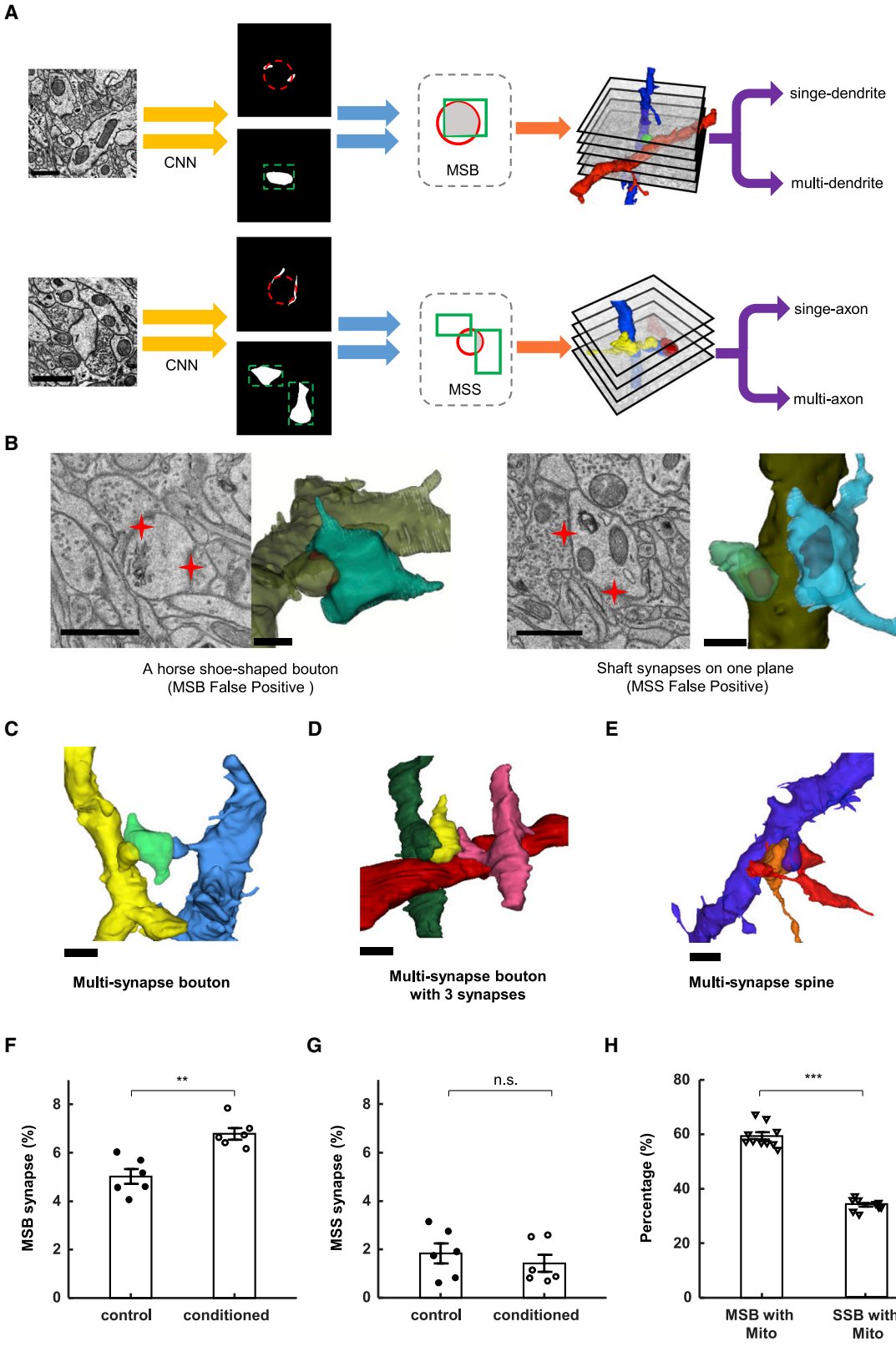

(legend on next page)

Combinatorial modeling to assess bouton and spine turnover patterns

Synapses undergo constant turnover in the adult brain, and long-term memory storage may involve formation of new synapses (Holtmaat et al., 2006; Kleim et al., 2002; Parkhurst et al., 2013; Xu et al., 2009; Yang et al., 2009, 2016). However, it is unclear to what extent such synaptic additions may be accompanied by elimination of existing synapses (or whether they tend to co-exist). We performed *in vivo* two-photon imaging of fluorescently labeled boutons and spines in the A1 of control and fear-conditioned mice and computed the long-term bouton and spine turnover rates 4 days after AFC. The formation and elimination rates of spines over the 4-day period were 9.7% ± 0.9% and 8.9% ± 0.4%, respectively (Mann-Whitney U test, $p = 0.89$; Figure 5A, left), and those of boutons were 14.7% ± 1.0% and 17.8% ± 1.2% (Mann-Whitney U test, $p = 0.06$; Figure 5A, right), with no significant net increase or decrease. We reasoned that, for any synapse, if addition of a new bouton/spine is always accompanied by elimination of the existing bouton/spine (Figure 5B, left), then the percentage of MCSs should remain constant, or otherwise there should be an increase in MCSs (Figure 5B, right). Thus, our finding that the percentage of MSSs remained unchanged after AFC (Figure 4G) suggests that new boutons tend to replace old ones, representing old connectivity patterns supplanted by new ones. In contrast, the significant increase in the number of MSBs (Figure 4F) suggests that new spines are added to existing synapses without eliminating old ones, representing addition of new connections while preserving old ones.

To quantitatively assess the difference in the turnover pattern of boutons and spines specifically to estimate the proportions of newly formed boutons/spines being replaced and/or added, we developed a combinatorial mathematical model that exhausted all turnover possibilities based on results from ssEM and long-term *in vivo* imaging (Figures 5C and 5D). We used the model to estimate (1) the proportion of boutons/spines for which formation was accompanied by elimination and (2) the proportion of boutons/spines that are simply added to existing synapses without eliminating old ones.

We took the MCS/1-to-1 synapse composition of control mice as the starting situation and that of conditioned mice as the end situation using a bipartite graph to model synaptic connections. To better reflect the difference in the MSB ratio before and after learning as well as to take into account computational complexity, we modeled using 120 synapses to obtain the final expected values, using combinatorics to calculate the possibility of different patterns. We assumed an equal possibility for all turnover patterns. The percentages of MSBs and MSSs and the elimination and formation rates of spines and boutons were based on experimental data (Figures 4F, 4G, and 5A). Synaptic turnover patterns that involve newly formed boutons/spines include the following 6 categories (− represents elimination and + formation):

$$\text{synaptic turnover}: \begin{cases} 1-\text{to}-1\ \text{synapse} \rightarrow 1-\text{to}-1\ \text{synapse}: \ -1\ \text{and}\ +1\ (A.) \\ \text{multiple}-\text{contact synapse} \rightarrow 1-\text{to}-1\ \text{synapse}: \ -2\ \text{and}\ +1\ (B.) \\ 1-\text{to}-1\ \text{synapse} \rightarrow \text{multiple}-\text{contact synapse}: \begin{cases} -0\ \text{and}\ +1\ (C.) \\ -1\ \text{and}\ +2\ (D.) \end{cases} \\ \text{multiple}-\text{contact synapse} \rightarrow \text{multiple}-\text{contact synapse}: \begin{cases} -1\ \text{and}\ +1\ (E.) \\ -2\ \text{and}\ +2\ (F.) \end{cases} \end{cases}$$

According to this classification, "synaptic replacement" includes (A.), (B.), (D.), (E.), and (F.), and "synaptic addition" includes only (C.). We built two models: one for bouton turnover and MSS and the other for spine turnover and MSB. These two models capture bouton and spine turnover

Figure 4. Synaptic organization in the A1

(A) MCS detection and classification. MCS candidates are first automatically marked based on a close vicinity criterion and then manually verified and classified as MSBs or MSSs by estimating the number of boutons based on vesicle cloud segmentation. Specifically, the bouton number is estimated by intersecting the fitting circle of the synapse and the bounding box of the vesicle cloud. Neurite reconstructions are then introduced to determine the origination of multiple spines or boutons. Red circles, fitted circles by synapse segmentation; green boxes, minimum boundary rectangles of vesicle cloud segmentation. Scale bar, 1 μm.

(B) Two examples of false positives identified by 3D reconstruction of synapses. The left subpanel shows an MSB false positive that was falsely detected because of the horseshoe-shaped bouton (dark green). The right subpanel shows an MSS false positive comprising two shaft synapses. Scale bar, 1 μm.

(C–E) Examples of a 3D-reconstructed MSB (C), an MSB with more than 2 postsynaptic sites (D), and an MSS (E). Scale bar, 1 μm.

(F) The percentage of MSB synapses is higher in conditioned mice (6.8% ± 0.2%) than in controls (5.0 ± 0.3%). n = 6 blocks, Mann-Whitney U test, $p < 0.01$.

(G) There is no difference in the percentage of MSS synapses between control (1.8% ± 0.4%) and conditioned mice (1.4% ± 0.3%). n = 6 blocks, Mann-Whitney U test, $p > 0.05$.

(H) The percentage of MSB synapses with presynaptic mitochondria (59.41% ± 1.3%) is higher than the percentage of SSB synapses with presynaptic mitochondria (34.12% ± 0.6%). n = 10 blocks, Mann-Whitney U test, $p < 0.001$.

See also Figure S4, Table S1, and Video S2.

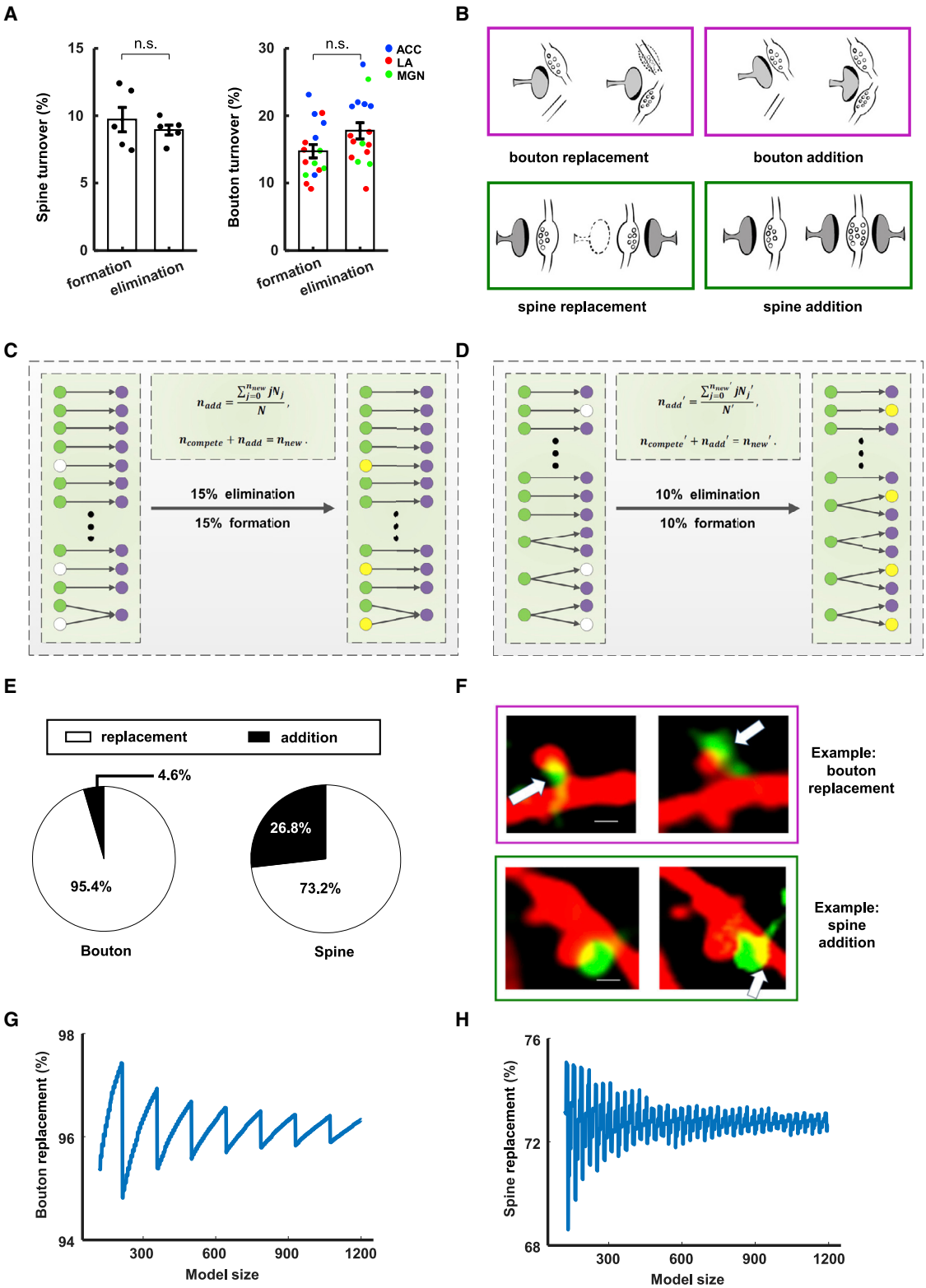

Figure 5. Synaptic turnover patterns

(A) Four-day turnover rates of spines (formation, 9.7% ± 0.9%; elimination, 8.9% ± 0.4%) and boutons (formation, 14.7% ± 1.0%; elimination, 17.8% ± 1.2%) in the auditory cortex of fear-conditioned mice (N = 5 mice). The bouton turnover rate is averaged among axons that project to the auditory cortex from the lateral

(legend continued on next page)

patterns, respectively (for the detailed calculation, see STAR Methods).

Our combinatorial mathematical modeling predicts a much higher percentage of replacement of boutons than of spines (Figures 5E, 5G, and 5H; STAR Methods), which is consistent with our observation *in vivo*. Among 856 putative synapses identified from two-photon imaging of the A1, there were 9 cases of a new bouton replacing an old bouton and 4 cases of a new spine adding onto an existing synapse; there were no cases where a new bouton was added to an existing synapse (Figure 5F). We attribute the low frequency of turnover events of MCSs in the *in vivo* dataset to the sparseness of neuronal labeling. These data suggest that each bouton tends to be the sole input of its postsynaptic counterpart, whereas spines can co-exist on a single bouton, suggesting that the information transfer pattern of "1-to-N" is more common than "N-to-1" in synaptic transmission.

Evaluating the information storage capacity of MSBs in static synaptic networks

Compared with two 1-to-1 synapses, two synapses formed by one MSB saved cellular resources required for two distinct presynaptic boutons. To further investigate the information coding capacity of MSBs, we developed a mathematical model to calculate the information storage capacity (ISC) (Chklovskii et al., 2004; Escobar et al., 2008; Stepanyants and Escobar, 2011; Stepanyants et al., 2002) of a synaptic network comprising a set number of synaptic connections. The ISC of a synaptic network is given by Shannon's information entropy (Shannon, 1948) H, which measures the average uncertainty in the synaptic connection patterns of the network and can be expressed as

$$H(X) = E[-\log_2 p(x)] = -\sum_{i=1}^{n} p(x_i)\log_2 p(x_i),$$

where n is the number of all possible connection patterns, X is a random variable of synaptic connection patterns, $p(x)$ is the probability mass function of X, and $p(x_i)$ is the probability measure of the occurrence of the i^{th} synaptic connection pattern x_i. We assume that the probability of each pattern of synaptic connection is equal and that the model transforms into a mode to solve for the number of eligible patterns. Here the degree of uncertainty in the network depends on the number of available dendrites to which each bouton could connect. For cases where the multiple postsynaptic structures of one MSB originate from the same dendrite, we consider the connection to be the same as a 1-to-1 synapse. Therefore, the ISC of an MSB synapse is determined by how many dendrites the MSB can connect to.

To determine the number of available dendrites for each bouton and the percentages of single-dendritic and multi-dendritic MSBs, we used the Multicut pipeline (Beier et al., 2017) and performed saturated reconstruction for two A1 tissue blocks of one control (22 × 24 × 25 μm) and one fear-conditioned (33 × 28 × 25 μm) mouse (Figures 6A and S5A; STAR Methods). Because the typical length of a spine (Bai et al., 2007) is 1 μm, we calculated the number of dendrites passing the vicinity of a bouton within a 1-μm radius in the reconstructed dataset (Figures 6B, S5B, and S5C; Video S3; STAR Methods). Among the 5,774 boutons analyzed, the median number of potential postsynaptic dendrites was 9 (Figure 6C), indicating that each bouton can potentially make synapses with 9 dendrites. We also traced each spine to its original dendrite to support categorization of MSB subtypes (single versus multi-dendritic). Contrary to previous *in vitro* results reporting that long-term potentiation (LTP) can lead to single-dendritic MSBs, generating stronger connections between pre- and post-synaptic neurons (Polsky et al., 2004), we found that more than 90% of MSBs were connected to multiple dendrites (Figure 6D), forming 1-to-N connections.

We then calculated the ISC of the synaptic network based on the synapse reconstruction results containing the following types of connections: (1) 1-to-1 synapses only, (2) 1-to-1 synapses and single-dendritic MSBs, and (3) 1-to-1 synapses and single- and multi-dendritic MSBs (Figure 6E). In a model with 100 synapses, of which 6% are MSB synapses (based on data from Figure 4F), single-dendritic MSB increased ISC by 2.5% over 1-to-1 synapses, and multi-dendritic MSB further increased 2.2%. The benefits of adding MSBs remained when the model was scaled up to 10^6 synapses (Figure 6F; STAR Methods). These results indicate that MSBs in a static network do increase information coding capacity but only slightly.

A plastic connectivity model for the ISC of synaptic networks

The percentage of multi-dendritic MSBs among all MSBs was higher in the conditioned mouse (95.1%) than in the control mouse (87.0%). This result, together with the percentages of MSBs in control and conditioned mice (5.0% ± 0.3% versus

amygdala (LA; N = 7 mice), anterior cingulate cortex (ACC; N = 5 mice), and medial geniculate nucleus (MGN; N = 4 mice). Mann-Whitney U test, $p > 0.05$, formation and elimination.

(B) Cartoons showing replacement and addition in bouton and spine turnover.

(C and D) Diagrams showing bouton (C) and spine (D) turnover in combinatorial mathematical models. Green, existing boutons; purple, existing spines; white, eliminated spine/bouton; yellow, added new spine/bouton; arrow, synaptic connection.

(E) Estimation of the percentage of replacement and addition for boutons (left) and spines (right) based on combinatorial mathematical modeling. Models predict 95.4% replacement of boutons and 73.2% replacement of spines.

(F) Synaptic turnover examples from *in vivo* two-photon microscopy analysis. Arrows point to elimination of an old bouton and formation of a new bouton (green, top) and to an addition of a new spine (red, bottom). Scale bar, 1 μm.

(G) The percentage of bouton replacement is around 96% when the model size is scaled up to 12,000 synapses.

(H) The percentage of spine replacement is around 72% when the model size is scaled up to 12,000 synapses.

See also Tables S1 and S2.

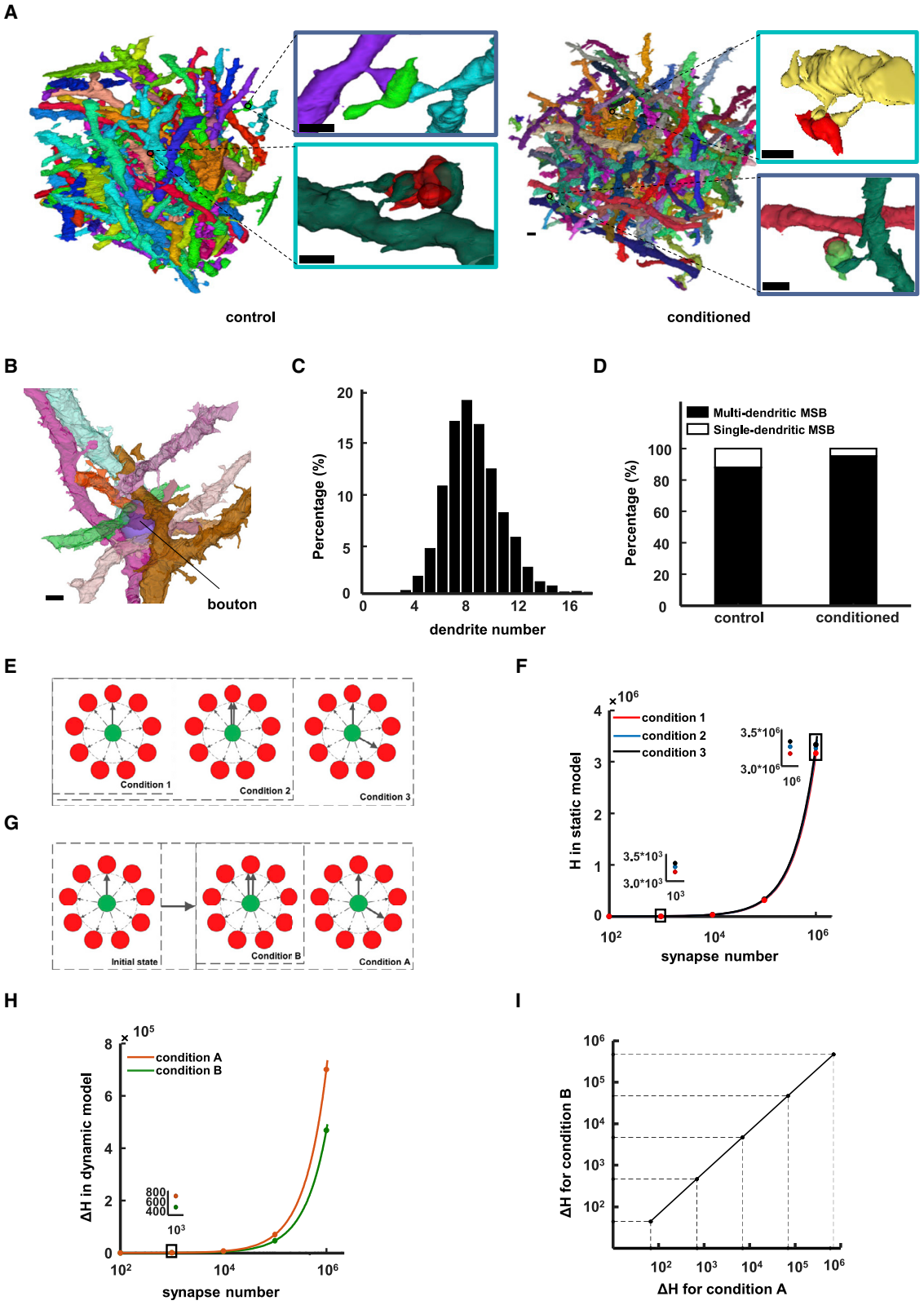

(legend on next page)

6.8% ± 0.2%; Figure 4F), indicates that essentially all of the MSBs newly formed after AFC were multi-dendritic. Thus, AFC resulted in boutons making novel connections with other dendrites rather than strengthening existing connections.

To evaluate the difference in ISC from establishment of new synaptic connections under the two conditions, multi-dendritic versus single-dendritic, we built a synaptic network model that incorporated synaptic plasticity by adding 10% more spines to the boutons (Figure 6G), based on the *in vivo* imaging results (Figure 5A). The increase in ISC depends on the number of new connections formed and the number of potential connection targets for each new connection. For newly formed multi-dendritic connections, the number of potential targets for each new connection is the number of dendrites with which a bouton can make contact (Figure 6C; condition A, forming multi-dendritic MSBs); for single-dendritic ones, the number of potential targets is 1 (condition B, forming single-dendritic MSBs).

The changes in ISC because of this 10% addition of synapses in the network, denoted by the increase of information entropy ΔH, were calculated for the condition A and condition B as follows:

$$\Delta H = H(Y) - H(X) = E[-\log_2 p(y)] - E[-\log_2 p(x)]$$
$$= -\sum_{i=1}^{m} p(y_i)\log_2 p(y_i) - \left(-\sum_{i=1}^{n} p(x_i)\log_2 p(x_i)\right),$$

where n and m are the number of all synaptic connection patterns before and after formation, respectively; Y and X are the random variables of the connection patterns after and before formation, respectively; $p(y)$ and $p(x)$ are the probability mass functions of Y and X, respectively; $p(y_i)$ is the probability of occurrence of the ith synaptic connection pattern after formation, y_i; and $p(x_i)$ is the probability of the ith connection pattern before formation x_i. We assume that the probability of each possible connection pattern is equal; the above dynamic model can also transform into a mode to solve for the number of eligible patterns.

Although a multi-dendritic MSB only slightly adds to the ISC in a static network (Figure 6F), in this plastic network, the increase in ISC for condition A was more than 50% higher (Figure 6H) than that of condition B. We found that this relative advantage for multi-dendritic connectivity scaled linearly with network size (Figure 6I). This result indicates that establishing new connections in a plastic network by forming multi-dendritic MSBs can increase information coding capacity significantly by 50%.

DISCUSSION

It is well established that learning can induce neuronal plasticity in the brain (Frank et al., 2018; Hayashi-Takagi et al., 2015; Holtmaat and Svoboda, 2009; Moczulska et al., 2013; Xu et al., 2009; Yang et al., 2009, 2016). In previous *in vivo* imaging studies, only a limited population of synapses was investigated, and it is not known how learning changes the shape and size of mitochondria in the brain. In this study, we used deep learning techniques to automatically detect synapses and mitochondria in ssEM images. This method allowed us to examine hundreds of thousands of synapses and mitochondria, and our results demonstrated that synaptic and mitochondrial organization were significantly affected by the learning process. With a particular focus on synapses consisting of multiple synaptic elements, we were able to identify a specific form of MCSs consisting of a single bouton and multiple spines from different dendrites, which were indicated by mathematical modeling to confer higher information storage than single-contact synapses.

We propose a 2D-3D pipeline to outline the 3D morphology of synapses from ssEM images. The first step focused on detecting and segmenting instances on 2D slices with advanced R-CNN, and the second converted the 2D instances into 3D individuals. Compared with other CNN techniques, the experimental results demonstrated that our method greatly improved detection and recall performance. For detection of MCSs, we first located them based on the close proximity criterion and then classified them into MSBs and MSSs using presynaptic vesicle information, another important feature for synapse identification (Dorkenwald et al., 2017). We obtained the dense reconstruction results by solving the graph partitioning problem so that the multiple spines of MSBs can be traced back to their original dendrites, enabling classification of MSB synapses based on their connectivity. However, the inherent error of our MCS detection algorithm is a limitation of this study, for which predicting the

Figure 6. Saturated reconstruction and ISC calculation

(A) Two reconstructed tissue blocks from control (left, 22 × 24 × 25 μm) and conditioned mice (right, 33 × 28 × 25 μm). Insets show examples of single- or multi-dendritic MSBs. Scale bar, 1 μm.

(B) A reconstructed example showing 10 dendrites intersecting within a 1-μm radius of a bouton. Scale bar, 1 μm.

(C) Distribution of the number of dendrites within a 1-μm radius of a bouton. n = 5,774 boutons.

(D) Percentage of single- and multi-dendritic MSBs in control (multi-dendrite MSBs, 86%) and conditioned (multi-dendrite MSBs, 95%) mice.

(E) Illustrations showing synaptic connectivity patterns of a static model. Condition 1, 1-to-1 synapses only; condition 2, 1-to-1 synapses and single-dendritic MSBs; condition 3, 1-to-1 synapses and single- and multi-dendritic MSBs.

(F) Information storage capacity (ISC) for static networks of different sizes for 3 conditions: 1-to-1 synapses only (condition 1), 1-to-1 synapses and single-dendritic MSBs (condition 2), and 1-to-1 synapses and single- and multi-dendritic MSBs (condition 3).

(G) Illustrations showing synaptic connectivity patterns of a plastic model. Condition A, multi-dendritic MSBs; condition B, single-dendritic MSBs only. Red, dendrite; green, bouton; solid arrow, one possible synaptic connection; dashed arrow, potential synaptic connection.

(H) Increase in ISC for plastic networks of different sizes for 2 conditions: new synapse on any passing dendrite (condition A) and new synapse on the same dendrite (condition B).

(I) Linear relationship for the increase in ISC for conditions A and B across different network sizes.

See also Figure S5, Table S3, and Video S3.

synaptic partner neurons with the CNN may be a solution in the future.

The unique shape of dendritic spines makes them easily identifiable (Gray, 1959; Peters and Kaiserman-Abramof, 1970); thus, spines have been studied extensively using *in vivo* imaging methods (Holtmaat et al., 2006; Svoboda and Yasuda, 2006). There are also synapses on dendritic shafts, which are not visible by fluorescent imaging but can be identified using our synapse classifier algorithms (Figures S6A–S6D) from ssEM images. The algorithms identified more shaft synapses in control animals than in conditioned animals (Figure S6E), which may be related to the homeostasis of cellular resource relocation.

The ssEM method enabled us to identify a special type of synapses, MCSs, containing MSSs or MSBs. An MSS can act as a coincidence detector when none of the boutons can activate the MSS alone. An MSS may also be activated preferentially by one bouton, leading to strengthening of one synapse and weakening of the others; eventually the MSS turns into a single-synaptic spine. Our finding that the number of MSSs stayed the same suggested that a new bouton outcompeted the previous bouton for being the sole input to the spine, changing the connection without adding MSSs. For MSBs, because a bouton can activate multiple spines, the new and old spines could form a stable synaptic configuration that allows information transfer from a single bouton to multiple spines. Because most MSBs made contact with more than one dendritic branch, information was broadcast from one neuron to multiple neurons. Our model indicated a 50% increase in ISC for multi-dendritic MSBs, which provides great potential for synaptic plasticity with a minimal increase in synapse number and structures. It is possible that such multi-dendritic MSB formation is common in learning paradigms that can lead to an increase in spine formation in relevant cortical areas (Frank et al., 2018; Hayashi-Takagi et al., 2015; Moczulska et al., 2013) because it is an energy-efficient way to add spines to existing neural circuits.

By design, our 2D-3D pipeline can be used to identify any cellular compartment or organelle with distinct structural properties, and we utilized it to identify mitochondria. In addition to generating energy for cellular functions, mitochondria play essential roles in regulating synaptic strength and plasticity by maintaining calcium homeostasis and controlling presynaptic vesicle release and cycling (Ly and Verstreken, 2006; Mironov and Symonchuk, 2006; Verstreken et al., 2005). There is also evidence suggesting that mitochondria adapt to the cellular energy requirements by highly dynamic fusion and fission (Berthet et al., 2014; Lewis et al., 2018; Westermann, 2012), and increasing mitochondrial fission can promote synapse formation (Dickey and Strack, 2011; Li et al., 2004). Given the direct relationship between presynaptic mitochondrial dynamics and the intensity and frequency of synaptic activities (Dubinsky, 2009), the increased number and decreased size of mitochondria we observed after fear conditioning may suggest an increase in presynaptic mitochondrial fission as a consequence of high calcium concentration caused by elevated synaptic activity (Lewis et al., 2018; Verstreken et al., 2005).

The recently reported connectome of 1 mm^3 human cerebral cortex (Shapson-Coe et al., 2021) shows the substantial improvement of EM imaging speed and the powerful ability of deep learning. In this study, rather than performing large-scale saturated reconstruction, we conducted specific and local classification of synapses and mitochondria, which allows ultrastructural analyses of specific cellular organelles without resource-demanding heavy computation. Because our method applies R-CNN to identify objects, it can potentially be used to extract other discrete, distinct structures from ssEM data, such as the Golgi apparatus and nucleus, making it a versatile tool for ssEM image processing.

Limitations of the study

In this study, we analyzed the ultrastructure of synapses and mitochondria in the mouse auditory cortex associated with fear learning; analyses of other brain regions for other learning paradigms may yield other biological findings but were not performed because of the workload. Partly because of the relatively thick serial sectioning (50 nm) and partly because of the lack of automated saturated reconstruction algorithms, we could not fully reconstruct all sample blocks, which limited our analyses, such as measuring dendritic distances between synapses. The thick serial sections also precluded us from identifying individual synaptic vesicles. Finally, we performed *in vivo* two-photon microscopy and EM on different animals. It will be of great value to analyze ultrastructural properties of synapses that have been imaged *in vivo*.

STAR★METHODS

Detailed methods are provided in the online version of this paper and include the following:

- KEY RESOURCES TABLE
- RESOURCE AVAILABILITY
  - Lead contact
  - Materials availability
  - Data and code availability
- EXPERIMENTAL MODEL AND SUBJECT DETAILS
  - Animals
- METHOD DETAILS
  - Behavior
  - Virus injection for *in vivo* imaging
  - Two-photon microscopy and data analysis
  - Electron microscopy sample preparation
  - Electron microscopy
  - Image alignment
  - Network architecture of U-Net, 3D U-Net and mask R-CNN
  - Block-wise inference strategy for large-scale data
  - 2D segmentation of neuronal processes
  - Automated volume segmentation
  - Experimental setup
  - Spine and shaft synapse classification
  - Error analysis of MCS detection algorithm
  - Mathematical modeling to assess bouton and spine turnover patterns: replacement/addition ratio
  - Calculating the number of dendrites intersecting within 1-μm radius of a bouton
  - Static synaptic connectivity model
  - Plastic synaptic connectivity model
- QUANTIFICATION AND STATISTICAL ANALYSIS

SUPPLEMENTAL INFORMATION

Supplemental information can be found online at https://doi.org/10.1016/j.celrep.2022.111151.

ACKNOWLEDGMENTS

We thank Drs. Mu-ming Poo, Ju Lu, Yi Zuo, and Margaret S. Ho for critical comments and suggestions. We also thank Linlin Li, Lina Zhang, Jingbin Yuan, and Jinyue Guo for technical support and Jie Luo, Jiazheng Liu, Yi Jiang, and Lu Wang for manual proofreading. We thank the Transdisciplinary Platform of Brain Functional Connectome and Brain-inspired Intelligence in Huairou Science City in Beijing for providing technical support and device resources. This work was supported by grants from the National Science and Technology Innovation 2030 Major Program (2021ZD0204503, 2021ZD0204500), the Strategic Priority Research Program of Chinese Academy of Sciences (XDB32030208, XDA16021104), the National Natural Science Foundation of China (32171461), and the Program of Beijing Municipal Science & Technology Commission (Z201100008420004) (to H.H.); the National Natural Science Foundation of China (31970960) and the startup funding from ShanghaiTech University (to Y.Y.); and the National Natural Science Foundation of China (61673381) (to Q.X.).

AUTHOR CONTRIBUTIONS

H.H., Q.X., and Y.Y. conceived and guided the project. J.Q., Y.Y., and Y.K. performed the animal experiments and provided the samples. H.M. conducted EM imaging. G.L. implemented the automated location and navigation system. X.C. performed alignment. J.L. and B.H. developed the algorithms. Z.L. established the mathematical models. L.S. and H.Z. performed visualization and video production. Y.Y., J.L., J.Q., and Z.L. wrote the manuscript with contributions from all authors.

DECLARATION OF INTERESTS

The authors declare no competing interests.

Received: September 29, 2021
Revised: May 20, 2022
Accepted: July 11, 2022
Published: August 9, 2022

REFERENCES

Abadi, M., Barham, P., Chen, J., Chen, Z., Davis, A., Dean, J., Devin, M., Ghemawat, S., Irving, G., and Isard, M. (2016). Tensorflow: a system for large-scale machine learning. In 12th USENIX Symposium on Operating Systems Design and Implementation (OSDI 16) (USENIX Association).

Bai, W., Zhou, X., Ji, L., Cheng, J., and Wong, S.T.C. (2007). Automatic dendritic spine analysis in two photon laser scanning microscopy images. Cytometry A *71A*, 818–826.

Beier, T., Pape, C., Rahaman, N., Prange, T., Berg, S., Bock, D.D., Cardona, A., Knott, G.W., Plaza, S.M., Scheffer, L.K., et al. (2017). Multicut brings automated neurite segmentation closer to human performance. Nat. Methods *14*, 101–102.

Berthet, A., Margolis, E.B., Zhang, J., Hsieh, I., Zhang, J., Hnasko, T.S., Ahmad, J., Edwards, R.H., Sesaki, H., Huang, E.J., and Nakamura, K. (2014). Loss of mitochondrial fission depletes axonal mitochondria in midbrain dopamine neurons. J. Neurosci. *34*, 14304–14317.

Bottou, L. (2012). Stochastic gradient descent tricks. In Neural Networks: Tricks of the Trade (Springer), pp. 421–436.

Bourne, J.N., and Harris, K.M. (2011). Coordination of size and number of excitatory and inhibitory synapses results in a balanced structural plasticity along mature hippocampal CA1 dendrites during LTP. Hippocampus *21*, 354–373.

Chen, X., Xie, Q., Shen, L., and Han, H. (2018). Morphology-retained non-linear image registration of serial electron microscopy sections. In 2018 25th IEEE International Conference on Image Processing (ICIP) (IEEE).

Chklovskii, D.B., Mel, B.W., and Svoboda, K. (2004). Cortical rewiring and information storage. Nature *431*, 782–788.

Çiçek, Ö., Abdulkadir, A., Lienkamp, S.S., Brox, T., and Ronneberger, O. (2016). 3D U-Net: learning dense volumetric segmentation from sparse annotation. In International Conference on Medical Image Computing and Computer-Assisted Intervention (Springer).

Dickey, A.S., and Strack, S. (2011). PKA/AKAP1 and PP2A/Bβ2 regulate neuronal morphogenesis via Drp1 phosphorylation and mitochondrial bioenergetics. J. Neurosci. *31*, 15716–15726.

Dorkenwald, S., Schubert, P.J., Killinger, M.F., Urban, G., Mikula, S., Svara, F., and Kornfeld, J. (2017). Automated synaptic connectivity inference for volume electron microscopy. Nat. Methods *14*, 435–442.

Dubinsky, J.M. (2009). Heterogeneity of nervous system mitochondria: location, location, location. Exp. Neurol. *218*, 293–307.

Escobar, G., Fares, T., and Stepanyants, A. (2008). Structural plasticity of circuits in cortical neuropil. J. Neurosci. *28*, 8477–8488.

Frank, A.C., Huang, S., Zhou, M., Gdalyahu, A., Kastellakis, G., Silva, T.K., Lu, E., Wen, X., Poirazi, P., Trachtenberg, J.T., and Silva, A.J. (2018). Hotspots of dendritic spine turnover facilitate clustered spine addition and learning and memory. Nat. Commun. *9*, 422.

Friedman, J.R., and Nunnari, J. (2014). Mitochondrial form and function. Nature *505*, 335–343.

Geinisman, Y., Berry, R.W., Disterhoft, J.F., Power, J.M., and Van der Zee, E.A. (2001). Associative learning elicits the formation of multiple-synapse boutons. J. Neurosci. *21*, 5568–5573.

Gray, E.G. (1959). Axo-somatic and axo-dendritic synapses of the cerebral cortex: an electron microscope study. J. Anat. *93*, 420–433.

Gray, E.G. (1969). Electron microscopy of excitatory and inhibitory synapses: a brief review. Prog. Brain Res. *31*, 141–155.

Hayashi-Takagi, A., Yagishita, S., Nakamura, M., Shirai, F., Wu, Y.I., Loshbaugh, A.L., Kuhlman, B., Hahn, K.M., and Kasai, H. (2015). Labelling and optical erasure of synaptic memory traces in the motor cortex. Nature *525*, 333–338.

Hayworth, K.J., Morgan, J.L., Schalek, R., Berger, D.R., Hildebrand, D.G.C., and Lichtman, J.W. (2014). Imaging ATUM ultrathin section libraries with WaferMapper: a multi-scale approach to EM reconstruction of neural circuits. Front. Neural Circuits *8*, 68.

He, K., Zhang, X., Ren, S., and Sun, J. (2016). Deep residual learning for image recognition. In Proceedings of the IEEE Conference on Computer Vision and Pattern Recognition (IEEE).

He, K., Gkioxari, G., Dollár, P., and Girshick, R. (2017). Mask r-cnn. In Proceedings of the IEEE International Conference on Computer Vision (IEEE).

Holtmaat, A., and Svoboda, K. (2009). Experience-dependent structural synaptic plasticity in the mammalian brain. Nat. Rev. Neurosci. *10*, 647–658.

Holtmaat, A., Wilbrecht, L., Knott, G.W., Welker, E., and Svoboda, K. (2006). Experience-dependent and cell-type-specific spine growth in the neocortex. Nature *441*, 979–983.

Imbrosci, B., Schmitz, D., and Orlando, M. (2022). Automated detection and localization of synaptic vesicles in electron microscopy images. eNeuro *9*. ENEURO.0400-20.2021.

Jagadeesh, V., Anderson, J., Jones, B., Marc, R., Fisher, S., and Manjunath, B. (2014). Synapse classification and localization in electron micrographs. Pattern Recognit. Lett. *43*, 17–24.

Jones, T.A., Klintsova, A.Y., Kilman, V.L., Sirevaag, A.M., Greenough, W.T., and memory. (1997). Induction of multiple synapses by experience in the visual cortex of adult rats. Neurobiol. Learn. Mem. *68*, 13–20.

Kasthuri, N., Hayworth, K.J., Berger, D.R., Schalek, R.L., Conchello, J.A., Knowles-Barley, S., Lee, D., Vázquez-Reina, A., Kaynig, V., Jones, T.R.,

et al. (2015). Saturated reconstruction of a volume of neocortex. Cell *162*, 648–661.

Kim, S.Y., Hsu, J.E., Husbands, L.C., Kleim, J.A., and Jones, T.A. (2018). Coordinated plasticity of synapses and astrocytes underlies practice-driven functional vicariation in peri-infarct motor cortex. J. Neurosci. *38*, 93–107.

Kleim, J.A., Freeman, J.H., Jr., Bruneau, R., Nolan, B.C., Cooper, N.R., Zook, A., and Walters, D. (2002). Synapse formation is associated with memory storage in the cerebellum. Proc. Natl. Acad. Sci. USA *99*, 13228–13231.

Kreshuk, A., Straehle, C.N., Sommer, C., Koethe, U., Knott, G., and Hamprecht, F.A. (2011). Automated segmentation of synapses in 3D EM data. In 2011 IEEE International Symposium on Biomedical Imaging: From Nano to Macro (IEEE).

Lewis, T.L., Kwon, S.-K., Lee, A., Shaw, R., and Polleux, F. (2018). MFF-dependent mitochondrial fission regulates presynaptic release and axon branching by limiting axonal mitochondria size. Nat. Commun. *9*, 5008.

Li, Z., Okamoto, K.-I., Hayashi, Y., and Sheng, M. (2004). The importance of dendritic mitochondria in the morphogenesis and plasticity of spines and synapses. Cell *119*, 873–887.

Lin, T.-Y., Maire, M., Belongie, S., Hays, J., Perona, P., Ramanan, D., Dollár, P., and Zitnick, C.L. (2014). Microsoft coco: common objects in context. In European Conference on Computer Vision (Springer).

Lin, T.-Y., Dollár, P., Girshick, R., He, K., Hariharan, B., and Belongie, S. (2017). Feature pyramid networks for object detection. In Proceedings of the IEEE Conference on Computer Vision and Pattern Recognition.

Liu, C., Yuen, J., and Torralba, A. (2011). Sift flow: dense correspondence across scenes and its applications. IEEE Trans. Pattern Anal. Mach. Intell. *33*, 978–994.

Lucchi, A., Smith, K., Achanta, R., Knott, G., and Fua, P. (2011). Supervoxel-based segmentation of mitochondria in em image stacks with learned shape features. IEEE Trans. Med. Imaging *31*, 474–486.

Lucchi, A., Becker, C., Neila, P.M., and Fua, P. (2014). Exploiting enclosing membranes and contextual cues for mitochondria segmentation. In International Conference on Medical Image Computing and Computer-Assisted Intervention (Springer).

Ly, C.V., and Verstreken, P. (2006). Mitochondria at the synapse. Neuroscientist *12*, 291–299.

Mironov, S.L. (2007). ADP regulates movements of mitochondria in neurons. Biophys. J. *92*, 2944–2952.

Mironov, S.L., Ivannikov, M.V., and Johansson, M. (2005). [Ca2+]i signaling between mitochondria and endoplasmic reticulum in neurons is regulated by microtubules. From mitochondrial permeability transition pore to Ca2+-induced Ca2+ release. J. Biol. Chem. *280*, 715–721.

Mironov, S.L., and Symonchuk, N. (2006). ER vesicles and mitochondria move and communicate at synapses. J. Cell Sci. *119*, 4926–4934.

Mishchenko, Y., Hu, T., Spacek, J., Mendenhall, J., Harris, K.M., and Chklovskii, D.B. (2010). Ultrastructural analysis of hippocampal neuropil from the connectomics perspective. Neuron *67*, 1009–1020.

Moczulska, K.E., Tinter-Thiede, J., Peter, M., Ushakova, L., Wernle, T., Bathellier, B., and Rumpel, S. (2013). Dynamics of dendritic spines in the mouse auditory cortex during memory formation and memory recall. Proc. Natl. Acad. Sci. USA *110*, 18315–18320.

Narasimha, R., Ouyang, H., Gray, A., McLaughlin, S.W., and Subramaniam, S. (2009). Automatic joint classification and segmentation of whole cell 3D images. Pattern Recognit. *42*, 1067–1079.

Oztel, I., Yolcu, G., Ersoy, I., White, T., and Bunyak, F. (2017). Mitochondria segmentation in electron microscopy volumes using deep convolutional neural network. In 2017 IEEE International Conference on Bioinformatics and Biomedicine (BIBM) (IEEE).

Parkhurst, C.N., Yang, G., Ninan, I., Savas, J.N., Yates, J.R., 3rd, Lafaille, J.J., Hempstead, B.L., Littman, D.R., and Gan, W.B. (2013). Microglia promote learning-dependent synapse formation through brain-derived neurotrophic factor. Cell *155*, 1596–1609.

Peters, A., and Kaiserman-Abramof, I.R. (1970). The small pyramidal neuron of the rat cerebral cortex. The perikaryon, dendrites and spines. Am. J. Anat. *127*, 321–355.

Peters, A., Josephson, K., and Vincent, S.L. (1991). Effects of aging on the neuroglial cells and pericytes within area 17 of the rhesus monkey cerebral cortex. Anat. Rec. *229*, 384–398.

Polsky, A., Mel, B.W., and Schiller, J. (2004). Computational subunits in thin dendrites of pyramidal cells. Nat. Neurosci. *7*, 621–627.

Quan, T.M., Hildebrand, D.G.C., and Jeong, W.-K. (2021). Fusionnet: a deep fully residual convolutional neural network for image segmentation in connectomics. Front. Comput. Sci. *3*, 613981.

Rodriguez-Moreno, J., Rollenhagen, A., Arlandis, J., Santuy, A., Merchan-Pérez, A., DeFelipe, J., Lübke, J.H.R., and Clasca, F. (2018). Quantitative 3D ultrastructure of thalamocortical synapses from the "Lemniscal" ventral posteromedial nucleus in mouse barrel cortex. Cereb. Cortex *28*, 3159–3175.

Rollenhagen, A., Sätzler, K., Rodríguez, E.P., Jonas, P., Frotscher, M., and Lübke, J.H.R. (2007). Structural determinants of transmission at large hippocampal mossy fiber synapses. J. Neurosci. *27*, 10434–10444.

Rollenhagen, A., Klook, K., Sätzler, K., Qi, G., Anstötz, M., Feldmeyer, D., and Lübke, J.H.R. (2015). Structural determinants underlying the high efficacy of synaptic transmission and plasticity at synaptic boutons in layer 4 of the adult rat 'barrel cortex. Brain Struct. Funct. *220*, 3185–3209.

Ronneberger, O., Fischer, P., and Brox, T. (2015). U-net: convolutional networks for biomedical image segmentation. In International Conference on Medical Image Computing and Computer-Assisted Intervention (Springer).

Sätzler, K., Söhl, L.F., Bollmann, J.H., Borst, J.G.G., Frotscher, M., Sakmann, B., and Lübke, J.H.R. (2002). Three-dimensional reconstruction of a calyx of Held and its postsynaptic principal neuron in the medial nucleus of the trapezoid body. J. Neurosci. *22*, 10567–10579.

Schaefer, S., McPhail, T., and Warren, J. (2006). Image deformation using moving least squares. In ACM SIGGRAPH 2006 Papers (Association for Computing Machinery), pp. 533–540.

Schmuhl-Giesen, S., Rollenhagen, A., Walkenfort, B., Yakoubi, R., Sätzler, K., Miller, D., von Lehe, M., Hasenberg, M., and Lübke, J.H.R. (2022). Sublamina-specific dynamics and ultrastructural heterogeneity of layer 6 excitatory synaptic boutons in the adult human temporal lobe neocortex. Cereb. Cortex *32*, 1840–1865.

Schoonover, C.E., Tapia, J.-C., Schilling, V.C., Wimmer, V., Blazeski, R., Zhang, W., Mason, C.A., and Bruno, R.M. (2014). Comparative strength and dendritic organization of thalamocortical and corticocortical synapses onto excitatory layer 4 neurons. J. Neurosci. *34*, 6746–6758.

Shannon, C.E. (1948). A mathematical theory of communication. Bell Syst. Tech. J. *27*, 379–423.

Shapson-Coe, A., Januszewski, M., Berger, D.R., Pope, A., Wu, Y., Blakely, T., Schalek, R.L., Li, P., Wang, S., and Maitin-Shepard, J. (2021). A connectomic study of a petascale fragment of human cerebral cortex. Preprint at bioRxiv. https://doi.org/10.1101/2021.05.29.446289.

Sorra, K.E., and Harris, K.M. (1993). Occurrence and three-dimensional structure of multiple synapses between individual radiatum axons and their target pyramidal cells in hippocampal area CA1. J. Neurosci. *13*, 3736–3748.

Spruston, N. (2008). Pyramidal neurons: dendritic structure and synaptic integration. Nat. Rev. Neurosci. *9*, 206–221.

Staffler, B., Berning, M., Boergens, K.M., Gour, A., van der Smagt, P., and Helmstaedter, M. (2017). SynEM, automated synapse detection for connectomics. Elife *6*, e26414.

Stepanyants, A., Hof, P.R., and Chklovskii, D.B. (2002). Geometry and structural plasticity of synaptic connectivity. Neuron *34*, 275–288.

Stepanyants, A., and Escobar, G. (2011). Statistical traces of long-term memories stored in strengths and patterns of synaptic connections. J. Neurosci. *31*, 7657–7669.

Svoboda, K., and Yasuda, R. (2006). Principles of two-photon excitation microscopy and its applications to neuroscience. Neuron *50*, 823–839.

Verstreken, P., Ly, C.V., Venken, K.J.T., Koh, T.W., Zhou, Y., and Bellen, H.J. (2005). Synaptic mitochondria are critical for mobilization of reserve pool vesicles at Drosophila neuromuscular junctions. Neuron *47*, 365–378.

Vos, M., Lauwers, E., and Verstreken, P. (2010). Synaptic mitochondria in synaptic transmission and organization of vesicle pools in health and disease. Front. Synaptic Neurosci. *2*, 139.

Westermann, B. (2012). Bioenergetic role of mitochondrial fusion and fission. Biochim. Biophys. Acta *1817*, 1833–1838.

Woolley, C.S., Wenzel, H.J., and Schwartzkroin, P.A. (1996). Estradiol increases the frequency of multiple synapse boutons in the hippocampal CA1 region of the adult female rat. J. Comp. Neurol. *373*, 108–117.

Xiao, C., Li, W., Deng, H., Chen, X., Yang, Y., Xie, Q., and Han, H. (2018). Effective automated pipeline for 3D reconstruction of synapses based on deep learning. BMC Bioinformatics *19*, 263.

Xu-Friedman, M.A., and Regehr, W.G. (2003). Ultrastructural contributions to desensitization at cerebellar mossy fiber to granule cell synapses. J. Neurosci. *23*, 2182–2192.

Xu, T., Yu, X., Perlik, A.J., Tobin, W.F., Zweig, J.A., Tennant, K., Jones, T., and Zuo, Y. (2009). Rapid formation and selective stabilization of synapses for enduring motor memories. Nature *462*, 915–919.

Yakoubi, R., Rollenhagen, A., von Lehe, M., Miller, D., Walkenfort, B., Hasenberg, M., Sätzler, K., and Lübke, J.H. (2019a). Ultrastructural heterogeneity of layer 4 excitatory synaptic boutons in the adult human temporal lobe neocortex. Elife *8*, e48373.

Yakoubi, R., Rollenhagen, A., von Lehe, M., Shao, Y., Sätzler, K., and Lübke, J.H.R. (2019b). Quantitative three-dimensional reconstructions of excitatory synaptic boutons in layer 5 of the adult human temporal lobe neocortex: a fine-scale electron microscopic analysis. Cereb. Cortex *29*, 2797–2814.

Yang, G., Pan, F., and Gan, W.-B. (2009). Stably maintained dendritic spines are associated with lifelong memories. Nature *462*, 920–924.

Yang, Y., Liu, D.-q., Huang, W., Deng, J., Sun, Y., Zuo, Y., and Poo, M.-m. (2016). Selective synaptic remodeling of amygdalocortical connections associated with fear memory. Nat. Neurosci. *19*, 1348–1355.

Yuste, R. (2015). From the neuron doctrine to neural networks. Nat. Rev. Neurosci. *16*, 487–497.

STAR★METHODS

KEY RESOURCES TABLE

REAGENT or RESOURCE	SOURCE	IDENTIFIER
Deposited data		
Mice brain synapse dataset	This paper	Zenodo: https://doi.org/10.5281/zenodo.6681172
Experimental models: Organisms/strains		
Mouse: Thy-YFP-H	The Jackon Laboratory	JAX:000664
Mouse: C57BL/6J	Slac Laboratroy Animals	N/A
Software and algorithms		
TrakEM2	ImageJ	https://imagej.net/plugins/trakem2/
Python version 3.5	Python Software Foundation	https://www.python.org
MATLAB R2018a	MathWorks	https://www.mathworks.com/
Synapse reconstruction	This paper	Zenodo: https://doi.org/10.5281/zenodo.6676997
Multicut	(Beier et al., 2017)	https://github.com/ilastik/nature_methods_multicut_pipeline

RESOURCE AVAILABILITY

Lead contact

Further information and requests for resources and reagents should be directed to and will be fulfilled by the lead contact, Yang Yang (yangyang2@shanghaitech.edu.cn).

Materials availability

This study did not generate new unique reagents.

Data and code availability

- The ultrastructural information of all reconstructed synapses has been deposited at Zenodo and is publicly available as of the date of publication. DOIs are listed in the key resources table. Electron microscopy data reported in this paper will be shared by the lead contact upon request.
- All original code has been deposited at Zenodo and is publicly available as of the date of publication. DOIs are listed in the key resources table.
- Any additional information required to reanalyze the data reported in this paper is available from the lead contact upon request.

EXPERIMENTAL MODEL AND SUBJECT DETAILS

Animals

C57BL/6J mice were purchased from SLAC Laboratory Animals (Shanghai, China). YFP-H line mice were obtained from the Jackson Laboratory (Bar Harbor, ME, USA). Mice were bred and housed in the animal facility of Shanghai Protein Center under a 12 h light-dark cycle (7 am-7 pm light). Eight-to twelve-week-old male and female mice (16 mice in total) were used in the two-photon imaging experiments. Six eight-week male mice (C57BL/6J) were used in the electron microscopy experiments. All procedures were approved by the Animal Committee of the Shanghai Tech University.

METHOD DETAILS

Behavior

Fear conditioning and behavioral test for the freezing response took place in different environments. Mice were handled prior to conditioning. A commercial fear conditioning apparatus (MED Associates Inc., St. Albans, VT, USA) was used for the fear conditioning and behavioral test. Before conditioning and testing, the apparatus was wiped clean with 70% ethanol. The conditioned stimulus (CS) is a series of 14 kHz beeps (interleaved 0.5 s on, 0.5 s off) at 80 dB, lasting 10s in total; the unconditioned stimulus (US) is a 0.6 mA foot

shock lasting 2 s. The sound co-terminates with the foot shock. For conditioned animals, CS-US pairing was presented 5 times with random intervals ranging from 60 to 90 s. For naive animals, CS was presented 5 times with random intervals, without presentation of US. The behavioral responses to CS were tested 1 day after conditioning for both groups, using CS lasting 60 s. All conditioned animals showed high levels of freezing when CS was played, and naive animals did not show a freezing response (Figure S1B).

Virus injection for *in vivo* imaging

The AAV-hSyn-EGFP and AAV-hSyn-tdTomato vectors were produced by Taitool Bioscience, Co., Ltd. (Shanghai, China). Virus injection was performed using a previously described protocol (Yang et al., 2016). Briefly, mice were anesthetized with sodium pentobarbital (7 mg/kg) and placed in a stereotaxic frame (RWD Life Sciences Co., Ltd., Shenzhen, China). For axonal labeling and imaging in the auditory cortex, 0.1–0.2 μL GFP or tdTomato viruses ($\sim 10^{13}$ virus particles per ml) were injected, using a glass micropipette with a Nanoject III micro-injector (Drummond Scientific Company, Broomall, PA, USA), into three different regions that project axons to the auditory cortex: lateral amygdala (LA, 1.0 mm from bregma, 3.25 mm lateral from the midline, 3.55 mm vertical from the cortical surface), anterior cingulate cortex (ACC, −1.00 mm from bregma, 0.5 mm lateral from the midline, and 1.5 mm vertical from the cortical surface), medial geniculate nucleus: (MGN, 3.2 mm from bregma, 2.0 mm lateral from the midline, and 2.8 mm vertical from the cortical surface).

Two-photon microscopy and data analysis

We performed cranial window implantation and two-photon imaging in mouse auditory cortex using previously described protocols (Yang et al., 2016). Mice were imaged 1 day before and 3 days after fear conditioning. All images were analyzed using ImageJ (NIH, Bethesda, MD, USA). Dynamic turnover assays of boutons and spines were based on comparison of the images collected at two different time points (3 days after *vs*. 1 day before conditioning). Percentages were normalized to the initial image taken at 1 day before conditioning. Turnover of boutons was calculated by averaging the turnover rates of LA, ACC and MGN axonal boutons in the auditory cortex. For the dual-color labeled images, potential bouton-spine pairs were visually identified when a presynaptic bouton and a postsynaptic spine overlaid in the image stacks (Yang et al., 2016).

Electron microscopy sample preparation

The mouse was deeply anesthetized with sodium pentobarbital (50 mg/kg, i.p.) and transcardially perfused with freshly prepared 4% paraformaldehyde and 0.5% glutaraldehyde (EM grade) in phosphate-buffered saline (PBS) 3 days after behavioral training. The brain was post-fixed in 2% paraformaldehyde and 2% glutaraldehyde overnight in a cold room. Coronal brain sections of 100 μm were cut using a vibratome (Leica Microsystems). Blocks of the auditory cortex (2.4–2.7 mm from bregma, 4.2–4.5 mm lateral from the midline) were dissected and embedded in resin for serial sectioning. Serial sections of the samples were continuously sectioned at 50 nm from the superficial regions of ACx (10–100 μm from the pial surface) to target L1 of ACx with an ATUMtome automated tape-collecting ultramicrotome (RMC, Boeckeler instruments Inc., Tucson, AZ, USA) and then collected onto a Kapton polyimide tape (8 mm wide and 100 μm thick). The tape with brain sections were then segmented and attached to 4-inch silicon wafers *via* double coated carbon conductive tape (TED Pella Inc, Redding, CA, USA). Lastly, the wafers were coated with 6 nm of carbon though an EM ACE60 high vacuum film deposition instrument (Leica Microsystems GmbH, Wetzlar, Germany) to prevent charging during scanning EM imaging (Figure 1).

Electron microscopy

The tape-collected ultra-thin sections were imaged on a Carl Zeiss Supra 55 scanning electron microscope (Carl Zeiss AG,. Oberkochen, Germany) using a secondary electron detection (9 kV accelerating potential, working distance of approximately 6.0 mm), with resolution of 2–4 nm/pixel and pixel dwelling time of 1.5 μs.

Image alignment

To correct for distortions of serial sections from automated tape-collecting ultramicrotome scanning electron microscopy (ATUM-SEM), we used a non-linear registration algorithm (Chen et al., 2018) to create 3D image stacks that retain the original morphology as much as possible. We assumed that the tissue deformations on different sections were independent. In order to extract reliable correspondences between adjacent sections, we used the dense correspondence matching SIFT-flow algorithm (Liu et al., 2011). Then, the corresponding points on different sections were simultaneously adjusted based on an energy function to retain the same x-y coordinates. In addition, the displacements of these corresponding points were constrained to be smooth and small, thereby restricting the non-linear deformation of the original images. Finally, with the displacement vector of the extracted corresponding points, the positions of the points in the original sections, as well as in the aligned images, were obtained. The Moving-Least-Square (MLS) method (Schaefer et al., 2006) was used to warp each section image. The deformation result produced by the MLS method was globally smooth, and the biological tissue could retain its shape as a result of the rigid local transformation.

Network architecture of U-Net, 3D U-Net and mask R-CNN

As illustrated in Figures S2D and S2E, U-Net and 3D U-Net both consist of an encoding path and a decoding path, with five and four resolution steps, respectively. Take U-Net as an example: in each resolution step of encoding path, there are two 3 × 3 convolutions

each followed by the activation function rectified linear unit (ReLU). A 2 × 2 maxpooling operation with stride 2 is applied to reach the down-sampling level. A 2 × 2 upsampling operation followed by the 2 × 2 convolution is applied to reach the up-sampling level. The factor of feature channel numbers between two adjacent levels is two. To combine information from different levels, an operation which concatenates the feature maps from the equal resolution steps is used as a long skip connection. To avoid a quite complex network, the starting number of feature channels for the first layer and network depth are designed to be smaller than 2D U-Net.

As illustrated in Figures 2B and S2F, Mask R-CNN is composed of four primary parts: backbone network, Region Proposal Network (RPN), Region-CNN (R-CNN) and Mask branch.

The backbone network extracts features from the entire image, and shares them with the other three parts. We used the FPN for detecting synapses at different scales. The FPN consists of a bottom-up pathway and a top-down pathway with lateral connections. The bottom-up pathway leverages the hierarchy of the natural pyramid features of the ResNet50, and the top-down pathway recovers the original resolution by using the upsampling layer step by step. On each level of the pyramid, the top-down pathway features will be fused (element-wise addition) with the bottom-up pathway features in the corresponding level. By constructing the feature pyramid, the lower-resolution feature maps contain more semantic information, while the higher-resolution feature maps contain more detailed information. The scale-space induced from the feature pyramid fits well with the object-space. Thus, the RPN and R-CNN predict the class and regress the bounding box of objects at different scale using feature maps at different levels of the pyramid. The same applies for the mask branch. Specifically, the feature pyramid has 5 levels and the corresponding object scales are 16, 32, 64, 128, 256, respectively.

There is a 3 × 3 convolution in the first layer of RPN followed by two 1 × 1 convolutions for region proposals classification (output channel: n×2) and regression (output channel: n×4). n denotes the number of aspect ratios of RPN anchors. In our case, n is set 3 for aspect ratios 0.5, 1 and 2. Above layers are applied to all levels of FPN to span 5 scales.

R-CNN first crops feature maps from corresponding levels of FPN based on the RoIs predicted from RPN using a RoIAlign layer with pool size 7 × 7. The fixed-size feature maps are then fed into two fully connected layers of 1024 units that finally branch into two output layers: RoIs classification and regression.

Same as R-CNN, Mask branch also utilizes RoIAlign layer (pool size 14 × 14) to extract fixed-size features maps based on the RoIs predicted from R-CNN. Then the RoI feature maps are fed into four consecutive 3 × 3 convolutions followed by a 2 × 2 deconvolution with stride of 2. Finally, a 1 × 1 convolution is used to map the feature channel to the number of classes, which is 2 in our case.

Block-wise inference strategy for large-scale data

Due to the constraints of the GPU, the inference was designed to proceed in a block-wise way for large-scale data (Figures S3B and S3C). The original images were first cropped into small patches (2,048 × 2,048) with overlaps (100 × 100), which were then fed into the trained network to generate detection boxes and segmentation masks. To obtain the connection relationship at the 3D level, we used a strategy which first fused the results on 2D and then connected the adjacent 2D layers to produce the 3D results.

To facilitate the description of our algorithm, we defined N_i as the number of detection boxes in the i-th layer, and D_{ij} represented the j-th synaptic detection box in the i-th layer:

$$D_{ij} = \left(x_{ij}^1, y_{ij}^1, x_{ij}^2, y_{ij}^2\right),$$

where x_{ij}^1, y_{ij}^1, x_{ij}^2, y_{ij}^2 represented the left-upper coordinate, left-upper coordinate, right-lower coordinate and right-lower coordinate, respectively; $D_i = \{D_{ij}, j = 1,2, \ldots, N_i\}$ denoted the set of all detection boxes on the i-th layer. C_{ij} represented the corresponding segmentation result of the j-th synapse in the i-th layer.$C_i = \{C_{ij}, j = 1,2, \ldots, N_i\}$ represented the set of all binary segmentation results in the i-th layer.

Single-layer fusion algorithm for detection and segmentation results

After obtaining the synaptic detection and the segmentation results of small patches by deep neural network, we stitched them to recover the original image size. At the overlapping region, there could be multiple different detection results for the same synapse. In this case, the synapse was repeatedly detected. Therefore, we designed an iterative 2D fusion algorithm to fuse the detection bounding boxes and corresponding segmentation masks in the overlapping areas. The main procedures are as follows:

Step 1: Construct the Intersection-over-Union (IoU) matrix S_i between all candidate detection boxes D_{ij} in the i-th layer. The S_i matrix can be formulated as:

$$S_i = \begin{pmatrix} s_{11}^i & s_{12}^i & \cdots & s_{1N_i}^i \\ s_{21}^i & s_{22}^i & \cdots & s_{2N_i}^i \\ \vdots & \vdots & \ddots & \vdots \\ s_{N_i1}^i & s_{N_i2}^i & \cdots & s_{N_iN_i}^i \end{pmatrix},$$

where s_{jk}^{i} represents the IoU of the j-th detection box and the k-th detection box, and the calculation formula can be expressed as follows:

$$s_{jk}^{i} = \frac{A(\cap\{D_{ij}, D_{ik}\})}{A(\cup\{D_{ij}, D_{ik}\})},\ j = 1, 2, \ldots, N_i,$$

where A is a function of calculating area. $\cap\{D_{ij}, D_{ik}\}$ and $\cup\{D_{ij}, D_{ik}\}$ represent the intersection and union of D_{ij} and D_{ik}, respectively. Obviously, $s_{jk}^{i} \varepsilon [0,\ 1]$. It is not difficult to find that S_i is a sparsely symmetric matrix with a main diagonal of 1.

Step 2: Find the coordinates of elements in S_i which are greater than the threshold θ_1. Let *Ind* be a set, then:

$$Ind = II_{\{S_i > \theta_1\}},$$

where II denotes the indicator function. This operation acts on each element of S_i and returns the row and column number *jk* satisfying the condition.

Step 3: For $\forall jk \in Ind$, merge D_{ij} and D_{ik} into a new detection box D_{ijk}. The coordinates of the new detection box are illustrated as follows:

$$D'_{ijk} = \left(\min\left(x_{ij}^{1}, x_{ik}^{1}\right), \min\left(y_{ij}^{1}, y_{ik}^{1}\right), \max\left(x_{ij}^{2}, x_{ik}^{2}\right), \max\left(y_{ij}^{2}, y_{ik}^{2}\right)\right).$$

Step 4: Update N_i and D_i, and repeat above steps until no box need to be merged.

Multilayer 3D connection algorithm

In order to obtain 3D synapses from the serial 2D segmentation results as well as screen out false positives, we develop and implement a 3D connection algorithm in the fine registered stacks according to the continuity of ssEM images and the spatial structural information of synapses. This procedure not only recovers synaptic morphology at the 3D level, but also assigns a unique label to each 3D synapse. The main steps are as follows:

Step 1: Construct the similarity matrix S^{it} between the synapses in the i-th layer and synapses in the t-th layer. S^{it} can be formulated as follows:

$$S^{it} = \begin{pmatrix} s_{11}^{it} & s_{12}^{it} & \cdots & s_{1N_i}^{it} \\ s_{21}^{it} & s_{22}^{it} & \cdots & s_{2N_i}^{it} \\ \vdots & \vdots & \ddots & \vdots \\ s_{N_i1}^{it} & s_{N_i2}^{it} & \cdots & s_{N_iN_i}^{it} \end{pmatrix},$$

where t = i+1. It should be noted that s_{pq}^{it} represents the ratio of the overlapping area between D_{ip} and D_{tq} to the minimum area of these two, and the calculation formula is:

$$s_{pq}^{it} = \frac{A(\cap\{D_{ip}, D_{tq}\})}{\min(A(D_{ip}), A(D_{tq}))}.$$

Step 2: Find the coordinates of elements of S_{it}, which are greater than the thresholdT_s, *i.e.*

$$Ind1 = II_{\{S^{it} > T_s\}},$$

where II denotes the indicator function. This operation acts on each element of S^{it} and returns the row and column number *pq* satisfying the condition.

Step 3: For $\forall pq \in Ind1$, assign the same and unique label value to C_{tq} and C_{ip}. Then, the binary segmentation is converted into a label image.

Step 4: Repeat above steps for all layers and obtain a labeled stack. Look through all the labels to check the number of layers L_t for each label t. If L^t is less than the predefined threshold T_k, then delete the corresponding segmentation C_{it} from the original results, which can be expressed as follows:

$$C_i = C_i / C_{it} .$$

After implementing the block-wise algorithm, we obtain the final result of each large image, where the same label value indicates the same synapse at the 3D level.

2D segmentation of neuronal processes

We extracted two volumes (2,048 × 2,048 × 50 voxels) from control and conditioned group as the training data for membrane detection and dense reconstruction. In the ground truth, voxels with the same value belong to the same neurite in 3D. Three experienced annotators labeled the dense labels with cross-validation.

FusionNet (Quan et al., 2021) was trained to predict the neuronal membrane. The training data was extracted from the volume segmentation dataset. Pixels that were labeled as background or at the edge of any adjacent neurite objects were collected as boundaries. The membrane probability maps obtained from the network were binarized with a threshold of 0.5, and morphologically dilated with a disk radius of 2 in order to dismiss the small cracks in membranes and avoid merge errors. A watershed algorithm was then used to obtain connected neuronal components.

Automated volume segmentation

The thickness of ssEM sections is a key factor for automatic reconstruction. High anisotropy brings more problems and challenges in learning the affinity between voxels along the z-direction. The state-of-the-art approach, which learns an affinity graph by 3D CNN, did not perform well on our dataset. Therefore, we used the Multicut pipeline (Beier et al., 2017) to analyze our data. We first applied a distance transform to generate superpixels in 2D slices. Subsequently, we constructed a 3D region adjacency graph to connect the superpixels in 2D slices as well as between sections. We then abstracted the graph as G(V, E), where the node set V denoted all the superpixels and the edge set E represented boundaries between adjacent superpixels. Then, a random forest classifier was trained to predict the scores (probability of whether an edge should be cut) of every edge in the graph to obtain a weighted un-directed graph (Figure S5A). We thus solved the graph partitioning problem with an approximate solution. Finally, we imported the segmentation results to the proofreading tool, and assigned the proofreading task to 6 experienced experimenters. The proofreading took about 4 weeks.

Experimental setup

All networks were implemented in Keras with Tensorflow (Abadi et al., 2016) as backend. Mask R-CNN was initialized by the pre-trained model on COCO dataset (Lin et al., 2014). A stochastic gradient descent algorithm (Bottou, 2012) with learning rate of 0.001 was used to optimize the networks. The number of training epochs was set as 30, with 1000 steps in each epoch. In each step, we trained 256 anchors for RPN and 200 RoIs for R-CNN. Non-maximum suppression thresholds to filter overlapping boxes for RPN and R-CNN were set as 0.7 and 0.3, respectively. To avoid overfitting, we used online data augmentation, including random rotation, random flipping and adding random noise for all training datasets. All training and inference procedures were performed on servers equipped with NVIDIA Tesla K40 GPUs.

As for the hyperparameters in 3D connection algorithm, there were two hyperparameters: T_s, the threshold for similarity of synapses; T_k, the threshold for the number of layers that synapses were retained. The choice of these two hyperparameters depends on the section thickness (in our case, thickness = 50 nm). The optional ranges of T_s and T_k are 0.3–0.7 and 2–4, respectively. To evaluate the model performances under different parameters, we plotted PR curves (Figure S3A) for parameters T_k ranging from 1 to 5. We concluded that in our dataset, $T_k = 2$ or 3 both give good performance, with $T_k = 2$ having better recall performance and $T_k = 3$ better precision.

Spine and shaft synapse classification

Excitatory and inhibitory synapses are classified according to some established criteria (Peters et al., 1991). Due to the low axial resolution, indistinct synaptic vesicles and symmetry/asymmetry of PSDs can't be used to identify the classes of synapses. Although it is generally believed that excitatory synapses are mostly located on spines, some studies have indicated that excitatory synapses can also form on dendritic shafts (Bourne and Harris, 2011), which cannot be quantified *in vivo* by counting spines using microscopy. Accordingly, based on the presence of postsynaptic mitochondria (Figure S6A) and the shape of postsynaptic structures (Figure S6B), we established some rules to classify the spine and shaft synapses (Figures S6C and S6D).

Previous studies have shown that there are very few mitochondria in dendritic spines, thus the absence of mitochondria can be used as one informative feature for spine identification. If no mitochondria are present in the postsynaptic site on any layer, the synapse is classified as a "spine synapse". If the proportion of mitochondria present on all layers is greater than 50%, the synapse is classified as a "shaft synapse". Since the sectioning orientation may lead to false negatives (*e.g.*, Figure S6B), we added a

morphological criterion, *i.e.*, whether the shape of the postsynaptic element is spiny or flat, for classification of remaining conditions. The mean change rate of postsynaptic areas from adjacent sections is defined as the shape factor—another informative feature for spine identification. A higher shape factor value (greater than 0.33) indicates a higher probability of existence of spines; a lower shape factor value indicates the presence of shafts (Figure S6B). The evaluation on the test dataset consisting of 559 synapses showed that our method yielded an accuracy rate of 0.95.

Error analysis of MCS detection algorithm

The multiple boutons or spines in a single MCS had to appear on the same section for them to be successfully identified by our semi-automatic MCS detection algorithm (Figure S4B). Indeed, a comparison against manually quantified MSB/MSS suggested that the our semi-automatic MCS detection algorithm had a false negative detection rate of 25% for two densely reconstructed image stacks (Figure S4C). The data in Figures 4F and 4G were adjusted accordingly.

Mathematical modeling to assess bouton and spine turnover patterns: replacement/addition ratio

Estimating bouton replacement and addition ratio by MSS percentages and bouton turnover rate

According to the ssEM data (Figure 4G), there were 1.8% MSS synapses in control animals and 1.4% in conditioned animals. Based on *in vivo* microscopic analysis (Figure 5A), the bouton elimination rate was approximately 15% and the formation rate was 15%. We built a model starting with 120 synapses consisting of 118 1-to-1 synapses (98.3%) and 2 MSS synapses (1 MSS; 1.7%, approximated to 1.8%), and ending with 120 synapses, also 118 1-to-1 synapses and 2 MSS synapse (1.7%, approximated to 1.4%). Note that in this model, the spine entities remained the same, and the number of boutons eliminated and the number newly formed were both 18 (120 × 15%) since the number of spines and MSSs were both constant. Three major assumptions were made: 1) each bouton forms at most one synapse (MSB is not considered in this model); 2) each spine contains 1 or 2 synapses (for simplicity of modeling, we do not consider MSS containing 3 or more synapses); 3) the elimination/formation of synapses is represented by the elimination/formation of boutons.

To count all possible bouton turnover patterns, we considered bouton elimination before formation. There were a total of 3 types of bouton elimination, with the number of each type denoted as $a_k(k = 1,2,3)$ and the number of corresponding formation patterns satisfying the end situation denoted as $b_k(k = 1,2,3)$. The three types are as follows:

(1) All 18 bouton eliminations are from 1-to-1 synapses (118 in total), $a_1 = C_{118}^{18}$; All 18 bouton formations occur on above alone spines, $b_1 = 1$;
(2) There are 17 eliminations from 1-to-1 synapses and 1 from MSS synapses (2 in total), $a_2 = C_{118}^{17}C_2^1$; 17 bouton formations on above alone spines and then another one on one of the 119 candidate 1-to-1 synapses (118–17 + 1+17) to form MSS, $b_2 = C_{119}^1$;
(3) There are 16 eliminations from 1-to-1 synapses and 2 eliminations from 1 MSS, $a_3 = C_{118}^{16}C_2^2$; 17 bouton formations on above alone spines and then another one on one of the 119 candidate 1-to-1 synapses (118–16 + 17) to form MSS, $b_3 = C_{119}^1$.

Thus, the total number of synaptic turnover patterns, denoted by N, can be calculated by:

$$N = \sum_{i=1}^{3} a_i b_i ,$$

Then, we calculate the formation ratio of (A.), (B.), (D.), (E.), (F.) *vs*. (C.), indicating the percentage of bouton replacement and addition in new synapses, respectively. Assuming that the possibility of each synaptic turnover pattern is equal, the mathematical expectation for the number of synapses corresponding to Situation (C.) in 18 new synapses, n_{add}, and the corresponding number of new synapses where bouton replacement occurs, $n_{replace}$, can be derived using the following equations:

$$n_{add} = \frac{\sum_{j=0}^{18} jN_j}{N'} ,$$

$$n_{replace} + n_{add} = 18 ,$$

where, $N_j(j = 0,1,2, \ldots,18)$ is the number of synaptic turnover patterns in which only j out of 18 new synapses belong to Situation (C.). As the number of MSS after learning is only one, there can be no more than 1 addition. So $N_2 = N_3 = \ldots = N_{17} = N_{18} = 0$. $N_j(j = 0,1)$ can be obtained as follows:

$$N_0 = N - \sum_{j=1}^{18} N_j ,$$

$$N_1 = a_2 C_{101}^1 + a_3 C_{102}^1 .$$

In order to gain a better understanding of the above formula, both items in N_1 are elaborated as follows. For elimination type (2), after adding one synapse to each of the 17 alone spines, the last formed synapse to be determined is randomly added to one of 101 1-to-1 synapses that have previously remained unchanged (118–17), so the number of patterns is calculated as $a_2C_{101}^1$. For elimination type (3), the last formed synapse to be determined is randomly added to one of 102 1-to-1 synapses that have previously remained unchanged (118–16), and thus the number of patterns is obtained as. $a_3C_{102}^1$.

Using the above equations, we determined that of the 18 new boutons, on average, 17.17 were accompanied by old bouton elimination (*i.e.*, replacement) and the other 0.83 were added to existing 1-to-1 synapses to form MSSs, accounting for 95.4 and 4.6%, respectively.

In addition, we extended the model programmatically to any size regarding the number of synapses. The input parameters of the program included only the ratio of multiple-contact synapses before and after learning, turnover rate, and the number of synapses. To test our model with different parameters: the last parameter is scaled up to 12,000 and the other parameters are fixed. In general, the obtained results with different model sizes were similar, as shown in Figure 5G and Table S2.

Estimating spine replacement and addition ratio by MSB percentages and spine turnover rate

According to the ssEM data (Figure 4F), 5.0 and 6.8% of all synapses were MSB synapses in control and conditioned animals, respectively. Based on *in vivo* imaging data (Figure 5A), spine turnover rate was approximately 10% for elimination and 10% for formation. The starting 120 synapses consisted of 114 1-to-1 synapses (95%) and 6 MSB synapses (3 MSBs; 5.0%), and the end situation consisted of 121 synapses including 12 new synapses (113 1-to-1 synapses and 8 MSB synapses, *i.e.*, 4 MSBs, 6.6%, approximated to 6.8%). It should be noted that in this model, the bouton entities remain the same, and the difference between the number of synapses eliminated (11) and the number newly formed (120 × 10% = 12) is due to the constant number of boutons and variable number of MSBs. Three major assumptions were made: 1) each spine forms at most one synapse (MSS is not considered in this model); 2) each bouton contains 1 or 2 synapses; 3) the elimination/formation of synapses is represented by the elimination/formation of spines.

To count all possible spine turnover patterns, we considered spine elimination before formation. There were a total of 10 types of spine elimination, with the number of each type denoted as $a'_k(k = 1, 2, \ldots, 10)$ and the number of corresponding formation patterns satisfying the end situation denoted as $b'_\kappa(k = 1, 2, \ldots, 10)$. The 10 types are as follows:

(1′) All 11 spine eliminations are from 1-to-1 synapses (114 in total), $a'_1 = C_{114}^{11}$; 11 out of 12 spine formations occur on above alone boutons and then another one on one of the 114 candidate 1-to-1 synapses (114–11 + 11) to form MSB, $b'_1 = C_{114}^1$;
(2′) There are 10 eliminations from 1-to-1 synapses and 1 from MSB synapses (6 in total), $a'_2 = C_{114}^{10}C_3^1C_2^1$; 10 spine formations on above alone boutons and then another two on 115 1-to-1 synapses (114–10 + 1+10), $b'_2 = C_{115}^2$;
(3′) There are 9 eliminations from 1-to-1 synapses and 2 eliminations from one single MSB, $a'_3 = C_{114}^9C_3^1C_2^2$; 10 spine formations on above alone boutons and then another two on 115 1-to-1 synapses (114–9+10), $b'_3 = C_{115}^2$;
(4′) 9 eliminations from 1-to-1 synapses and 2 eliminations from two different MSBs, $a'_4 = C_{114}^9C_3^2(C_2^1)^2$; 9 spine formations on above alone boutons and then another three on 116 1-to-1 synapses (114–9+2 + 9), $b'_4 = C_{116}^3$;
(5′) There are 8 eliminations from 1-to-1 synapses and 3 eliminations from MSBs, of which 2 are on the same MSB, $a'_5 = C_{114}^8C_3^1C_2^2C_2^1C_2^1$; 9 spine formations on above alone boutons and then another three on 116 1-to-1 synapses (114–8+1 + 9), $b'_5 = C_{116}^3$;
(6′) There are 8 eliminations from 1-to-1 synapses and 3 eliminations from different MSBs, $a'_6 = C_{114}^8C_3^3(C_2^1)^3$; 8 spine formations on above alone boutons and then another four on 117 1-to-1 synapses (114–8+3 + 8), $b'_6 = C_{117}^4$;
(7′) There are 7 eliminations from 1-to-1 synapses and 4 eliminations from 2 MSBs, $a'_7 = C_{114}^7C_3^2(C_2^2)^2$; 9 spine formations on above alone boutons and then another three on 116 1-to-1 synapses (114–7+9), $b'_7 = C_{116}^3$;
(8′) There are 7 eliminations from 1-to-1 synapses and 4 eliminations from 3 MSBs, $a'_8 = C_{114}^7C_3^1C_2^2C_2^2(C_2^1)^2$; 8 spine formations on above alone boutons and then another four on 117 1-to-1 synapses (114–7+2 + 8), $b'_8 = C_{117}^4$;
(9′) There are 6 eliminations from 1-to-1 synapses and 5 eliminations from 3 MSBs, $a'_9 = C_{114}^6C_3^2(C_2^2)^2C_2^1$; 8 spine formations on above alone boutons and then another four on 117 1-to-1 synapses (114–6+1 + 8), $b'_9 = C_{117}^4$;
(10′) There are 5 eliminations from 1-to-1 synapses and 6 eliminations from 3 MSBs, $a'_{10} = C_{114}^5C_3^3(C_2^2)^3$; 8 spine formations on above alone boutons and then another four on 117 1-to-1 synapses (114–5+8), $b'_{10} = C_{117}^4$.

Therefore, the total number of synaptic turnover patterns, denoted by N', can be calculated by:

$$N' = \sum_{i=1}^{10} a'_i b'_i ,$$

Then, we calculate the formation ratio of (A.), (B.), (D.), (E.), (F.) *vs*. (C.), indicating the percentage of spine replacement and addition in new synapses, respectively. Assuming that the possibility of each synaptic turnover pattern is equal, the mathematical expectation for the number of synapses corresponding to Situation (C.) in 12 new synapses, n'_{add}, and the corresponding number of new synapses where spine replacement occurs, $n'_{replace}$, can be derived from the following equations:

$$n'_{add} = \frac{\sum_{j=0}^{12} jN'_j}{N'} ,$$

$$n'_{replace} + n'_{add} = 12 ,$$

where, $N'_j(j = 0, 1, 2, \ldots, 12)$ is the number of synaptic turnover patterns in which only j out of 12 new synapses belong to Situation (C.). As the number of MSBs after learning is 4, there can be no more than 4 additions. So, $N'_5 = N'_5 = \ldots = N'_{11} = N'_{12} = 0$. $N'_j(j = 0, 1, \ldots, 4)$ can be obtained as follows:

$$N'_0 = N' - \sum_{j=1}^{12} N'_j ,$$

$$N'_1 = a'_1 C^1_{103} + a'_2 C^1_{104} C^1_{11} + a'_3 C^1_{105} C^1_{10} + a'_4 C^1_{105} C^2_{11} + a'_5 C^1_{106} C^2_{10} + a'_6 C^1_{106} C^3_{11} + a'_7 C^1_{107} C^2_9 + a'_8 C^1_{107} C^3_{10} + a'_9 C^1_{108} C^3_9 + a'_{10} C^1_{109} C^3_8 ,$$

$$N'_2 = a'_2 C^2_{104} + a'_3 C^2_{105} + a'_4 C^2_{105} C^1_{11} + a'_5 C^2_{106} C^1_{10} + a'_6 C^2_{106} C^2_{11} + a'_7 C^2_{107} C^1_9 + a'_8 C^2_{107} C^2_{10} + a'_9 C^2_{108} C^2_9 + a'_{10} C^2_{109} C^2_8 ,$$

$$N'_3 = a'_4 C^3_{105} + a'_5 C^3_{106} + a'_6 C^3_{106} C^1_{11} + a'_7 C^3_{107} + a'_8 C^3_{107} C^1_{10} + a'_9 C^3_{108} C^1_9 + a'_{10} C^3_{109} C^1_8 ,$$

$$N'_4 = a'_6 C^4_{106} + a'_8 C^4_{107} + a'_9 C^4_{108} + a'_{10} C^4_{109} .$$

The first three items in N'_1 are selected for detailed explanation. For elimination type (1′), after adding one synapse to each of the 11 alone boutons, the last formed synapse to be determined is randomly added to one of 103 1-to-1 synapses that have previously remained unchanged (114–11), and therefore the number of patterns is obtained as $a'_1 C^1_{103}$. For elimination type (2′), the last two newly formed synapses to be determined are randomly added to one of 104 1-to-1 synapses that have previously remained unchanged (114–10) and one of other 11 "new" 1-to-1 synapses (10 1-to-1 synapses formed by 1 elimination of old 1-to-1 synapses and subsequent 1 addition; 1 1-to-1 synapse by eliminating 1 synapse of MSB), respectively. So, the number of patterns is calculated as $a'_2 C^1_{104} C^1_{11}$. For elimination type (3′), the last two new synapses to be determined are randomly added to one of 105 1-to-1 synapses that have previously remained unchanged (114–9) and one of other 10 "new" 1-to-1 synapses (9 formed by 1 elimination of old 1-to-1 synapses and subsequent 1 addition; 1 formed by 2 synaptic elimination of an old MSB and subsequent 1 addition), respectively. So, the number of patterns is obtained as $a'_3 C^1_{105} C^1_{10}$.

Using the above equations, we determined that of the 12 new spines, on average, 8.78 were accompanied by old spine elimination (i.e., replacement) and the other 3.22 were added to existing 1-to-1 synapses to form MSBs, accounting for 73.2 and 26.8%, respectively.

In addition, we also developed the model programmatically for any model size about the number of synapses. In general, the obtained results with different model sizes are similar, as shown in Figure 5H and Table S2.

Calculating the number of dendrites intersecting within 1-μm radius of a bouton

Based on the dense reconstruction results, we formulated some criteria to identify each neurite as dendritic or not. We extracted a 2D vector (number of voxels and ratio of vesicle cloud) as features to classify the segments. If the number of voxels in a neurite was greater than 250,000 and the ratio of vesicle cloud in it was less than 5%, this neurite was classified as dendritic (Figures S5B and S5C). For each bouton, we fit a minimum circumscribed circle and obtained the radius (R) and center (x, y, z) approximately. Then, we extended a sphere centered on (x, y, z) with radius of R+1 μm, and the number of dendrites that pass through the sphere was calculated.

Static synaptic connectivity model

For simplicity, our static model consists of 100 synaptic connections (Figure 6E). Based on our experimental data (Figure 6C), each bouton can make contact with its 9 potential dendrites. There are two notable constraints: 1) at most 2 synapses can be formed per bouton; 2) 6% of the synapses are MSB synapses (Figure 4F) for conditions 2 and 3.

For condition 1, the constraint of the number of synapses and only one synapse formed per bouton makes the existence of exactly 100 boutons. Each independent bouton has C^1_9 possible connections, so there is a total of $(C^1_9)^{100}$ patterns for condition 1. For condition 2, since 6% of synapses are MSB synapses, there are a total of 6 MSB synapses from 3 MSBs. Thus, this condition consists of 97 boutons including 94 1-to-1 boutons and 3 MSBs. Accordingly, the number of patterns for condition 2 can be given by $C^3_{97}(C^1_9)^{94}(C^1_9)^3$. In other words, the selection of 3 MSBs from 97 boutons and the independent connection of each bouton are all factors that contribute to the increase of the number of patterns. For condition 3, each of the 3 boutons selected as MSBs has

$(C_9^2 + C_9^1)$ optional connection patterns that meet the condition. Rethinking the consideration of condition 2, the total number of patterns that meet condition 3 can be calculated as. $C_{97}^3 (C_9^1)^{94} (C_9^2 + C_9^1)^3$.

In detail, we express the respective calculation equations of information entropy that satisfy conditions 1, 2 and 3, as follows:

$$H_{condition1} = -\sum_{i=1}^{(C_9^1)^{100}} \frac{1}{(C_9^1)^{100}} \log_2 \frac{1}{(C_9^1)^{100}} = 317 bits\ ,$$

$$H_{condition2} = -\sum_{i=1}^{C_{97}^3 (C_9^1)^{97}} \frac{1}{C_{97}^3 (C_9^1)^{97}} \log_2 \frac{1}{C_{97}^3 (C_9^1)^{97}} = 325 bits\ ,$$

$$H_{condition3} = -\sum_{i=1}^{C_{97}^3 (C_9^1)^{94} (C_9^2 + C_9^1)^3} \frac{1}{C_{97}^3 (C_9^1)^{94} (C_9^2 + C_9^1)^3} \log_2 \frac{1}{C_{97}^3 (C_9^1)^{94} (C_9^2 + C_9^1)^3} = 332\ bits\ ,$$

where, C_n^m is the combinatorial number with respect to n and m.

Thus, including an MSB that connect to the same dendrite increases the ISC by 2.5% in this model, and the connectivity of the MSB to multiple dendrites increases another 2.2%. The results hold when we scale up the model tenfold each time up to 10^6 synapses (Figure 6F). The information entropy values of 3 conditions under 5 model scales are listed in Table S3. The benefits of adding MSBs remained when the model was scaled up to 10^6 synapses (Figure 6F).

Plastic synaptic connectivity model

We built a neural network model that incorporated plasticity by adding 10% more contacts to the boutons as a form of learning-induced synaptic formation. Plasticity is represented by a 10% increase in synaptic connections by adding 10 connections to existing boutons in a network consisting of 100 boutons and 100 1-to-1 synapses. There are two notable constraints: 1, at most one synapse is added to each bouton; 2, formation of the new synapses is random.

Before the synaptic formation, the number of possible connections for both conditions A and B was $(C_9^1)^{100}$, which is the same as condition 1 of the static model. For condition B, new connections can only be formed on the same dendrite. Therefore, only the factor of the selection of the 10 boutons from the 100 boutons to form new synapses can lead to an increase in the number of patterns triggered by the synaptic formation. Furthermore, the number of patterns after formation can be written as $C_{100}^{10} (C_9^1)^{90} (C_9^1)^{10}$. For condition A, like condition 3 in the static model, each of the 10 boutons selected as MSBs has $(C_9^2 + C_9^1)$ optional connection patterns that meet the criterion. Rethinking the consideration of condition B, the total number of patterns that meet condition A can be calculated as $C_{100}^{10} (C_9^1)^{90} (C_9^2 + C_9^1)^{10}$. We can obtain the increase of information entropy for conditions A and B, as follows:

$$\Delta H_{conditionA} = -\sum_{i=1}^{C_{100}^{10} (C_9^1)^{90} (C_9^2 + C_9^1)^{10}} \frac{1}{C_{100}^{10} (C_9^1)^{90} (C_9^2 + C_9^1)^{10}} \log_2 \frac{1}{C_{100}^{10} (C_9^1)^{90} (C_9^2 + C_9^1)^{10}} - \left(-\sum_{i=1}^{(C_9^1)^{100}} \frac{1}{(C_9^1)^{100}} \log_2 \frac{1}{(C_9^1)^{100}} \right)$$
$$= 67\ bits\ ,$$

$$\Delta H_{conditionB} = -\sum_{i=1}^{C_{100}^{10} (C_9^1)^{100}} \frac{1}{C_{100}^{10} (C_9^1)^{100}} \log_2 \frac{1}{C_{100}^{10} (C_9^1)^{100}} - \left(-\sum_{i=1}^{(C_9^1)^{100}} \frac{1}{(C_9^1)^{100}} \log_2 \frac{1}{(C_9^1)^{100}} \right) = 44\ bits\ .$$

Clearly, in a plastic network, the possibility of a bouton connecting to multiple dendrites dramatically increases the information entropy added by synaptic plasticity. The results hold when we scale up the model tenfold each time up to 10^6 synapses (Figure 6H). The increase of information entropy values of 2 conditions under 5 model scales is shown in Table S3. Notably, whereas multi-dendritic MSB only slightly adds to the ISC in a static network (Figure 6F), the increase in the ISC for condition A by adding synapses is more than 50% (Figure 6H) higher than that of condition B in the plastic network. The relative advantage of multidendritic connectivity in ΔH scaled linearly with the network size (Figure 6I).

QUANTIFICATION AND STATISTICAL ANALYSIS

Statistical analyses were conducted using MATLAB R2018a. Sample size: 14 tissue blocks in electron microscopy experiments; 16 mice in two-photon imaging experiments. Data were presented as mean ± SEM, where N is the number of mice or tissue blocks (indicated in Figure legends). For Figure 2E, two-sided Kolmogorov-Smirnov test; for independent group comparison between tissues from control and conditioned mice (Figures 3D–3F, 4F–4H, S3J, S4D and S6E), Mann Whitney U test; for the comparison of spine/bouton formation and elimination rates in two-photon imaging experiments (Figure 5A), Mann Whitney U test; for freezing response comparison between control and condition mice after conditioned stimulus (Figure S1B), Student's t-test. In figures, asterisks stand for: *$p < 0.05$, **$p < 0.01$,***$p < 0.001$.